Low-Frequency Piezoelectric Energy Harvester with Novel 3D Folded Zigzag Design and High Power Density

by

Dilpreet S. Bath

A thesis
presented to the University of Waterloo
in fulfillment of the
thesis requirement for the degree of
Masters of Applied Science
in
Mechanical and Mechatronics Engineering

Waterloo, Ontario, Canada, 2018

Author's Declaration

I hereby declare that I am the sole author of this thesis. This is a true copy of the thesis, including any required final revisions, as accepted by my examiners.

I understand that my thesis may be made electronically available to the public.

Abstract

Cantilevers have been widely used for vibration energy harvesting applications using piezoelectric materials due to their simple geometries, frequency tune-ability, and closed form analytical solution. Recent studies have focused on overcoming some of the drawbacks for this configuration, which include low power density and natural frequencies much higher than those available in the environment. Some have investigated two-dimensional geometries, such as a zigzag shaped design, or meandering or elephant design. The previously researched designs offer a higher flexibility that allows for much smaller fundamental natural frequencies, and hence, improved power densities. The presented work extends this idea by offering a novel, three-dimensional design called "folded zigzag" that provides a much better flexibility than the aforementioned units, and aids significantly with natural frequency requirements while having a small footprint.

The research compares the proposed design to the planar symmetric zigzag design for the same footprint area. This paper demonstrates that the proposed geometry offers a much lower resonating frequency, and results in much improved strain node geometry by avoiding torsion in the fundamental modes of operation. This significantly eases the fabrication by avoiding charge cancellations when mounting continuous electrodes. In addition to that, the new design being more flexible due to its geometry, has higher strain, producing a larger voltage. The graphs produced using validated simulations compare the power densities of various designs. More specifically, the proposed design's power density is compared to the conventional planar symmetric zigzag design's power density. The results show that the individual layers of the new design can produce higher power density than a planar symmetric zigzag.

This work also outlines the manufacturing process used to fabricate a folded zigzag design with piezoelectric material, which involves strain matching the electrodes, on both the top and bottom layer. Overall, not only is the folded zigzag design more resistant to the formation of strain nodes than the planar zigzag design but it also produces higher power at a low natural frequency, making it suitable for wireless sensor technology and other applications.

Acknowledgements

Table of Contents

List of Figures

List of Tables

Chapter 1
Introduction

This chapter introduces the motivation, background and contribution of the research presented in this thesis. It also describes the major contributions of the research to its related fields and sets the scope for upcoming topics.

1.1 Motivation

With the ever-growing demand for infrastructures such as buildings, bridges, and pipelines, there has been an increasing need to monitor their physical health. As a result, there have been advancements in the "Wireless Sensor Network (WSN)" systems to achieve this goal. A WSN is the random deployment of sensors in inaccessible locations to sense, record and transmit the physical or environmental data of the surroundings [1]. The major applications for this technology include structural health monitoring (SHM), smart grid, temperature monitoring, and various military applications [1]. As the deployment region for these networks becomes more remote and inaccessible, the maintenance cost rises as well. This is primarily because the power unit, such as a battery, used to run the sensor requires regular replacement. In order to eliminate this drawback, there has been a shift towards the modernized "self-sustained" sensors. These sensors use energy harvesters for their power requirements, hence eradicating the need for constant power unit replacement. Based on their applications, different energy harvesting techniques are used to power the sensor. Interestingly enough, the use of ambient vibrations to power the WSN has received significant attention in the past decade. Hence, the main motivation for improving this technology is powering these sensor modules using the energy harvested from ambient vibrations for applications such as Structural Health Monitoring [2]–[5]. Unfortunately, implementing these energy harvesters (EH) into sensor modules is still an ongoing process due to the challenges faced by the designs. The most significant are the low power density and high natural frequency due to the size constraints and the level and quality of vibrations available from the surroundings [6]. Considering these issues, there is a need to develop a new design for an energy harvester with a low natural frequency and high power density.

1.2 Scope of Research

The purpose of this research is to design a novel energy harvester with a low natural frequency and high power density. With the ambient environment as the energy source, the resonance based energy harvester is designed to harvest energy from frequencies less than 100 Hz as a study conducted by Reilly et al. shows that the natural frequency of majority of the ambient vibrations in industrial, residential and various other settings is less than 100 Hz [7]. In addition, the increasing need to decrease the size of a Micro Electro-Mechanical System (MEMS) scale energy harvester for integration into a sensor module results in a higher natural frequency. To overcome these challenges, a novel 3D design of an energy harvester is introduced and analyzed numerically and experimentally. Furthermore, the proposed design is compared to the state-of-the-art zigzag design by Karami *et al.* to show its advantages in terms of power density and natural frequency.

A finite element model (FEM) is developed to predict the mechanical and electrical behaviour of the proposed design. The dynamic behaviour of the design is quantified by performing a variety of design altercations. In addition to that, COMSOL is used to perform load sweep analysis in order to evaluate the optimal resistance and power output from the design. Finally, conclusions are drawn from simpler geometry models after validating the complex numerical models using experiments.

1.3 Contribution

This research explores the design of a low frequency energy harvester that can potentially be used as a power source for wireless sensor nodes. This novel design offers flexibility in terms of the number of legs, and layers as well as the distance between the layers to design the harvester for specific applications. COMSOL simulations are employed to study the dynamic behaviour of the proposed design in terms of strain node generation and natural frequency analysis. Additional simulations are performed to show the effect of the number of layers and the distance between the layers on the dynamics of the system. This thesis uses a numerical and experimental approach to model and analyze a two-layered design. Validated COMSOL model is used to compare the power density of the proposed design with the previous designs to show the advantages of the new geometry.

1.4 Thesis Outline

A summary of the 10 chapters is provided in this section:

Chapter 2 is divided into three different subsections, the first of which overviews the different methods used to harvest energy from vibrations. This provides additional information to understand the advancements made in this field. The next subsection goes over a simple cantilever based energy harvester in order to help the reader appreciate the piezoelectric aspect of vibrational energy harvesting. The final subsection covers the state of the art geometries used for low frequency piezoelectric energy harvesting.

Chapter 3, which discusses the criteria and constraints imposed on the design goes over the current requirements for the energy harvester and their desired qualities. The second subsection talks about the initial phase of the design and primary motivation. The last section introduces the final geometry of the proposed design and discusses about its advantages.

Chapter 4 outlines the numerical simulation used to analyze the proposed design. This section goes over different modules of COMSOL used to model the substrate and the piezo material. It also lists the geometric properties of the substrate and the piezoelectric material along with the boundary conditions used for modelling. The concept of strain matching the electrodes is also introduced in this section, which is discussed in detail in the manufacturing chapter. Finally, the expressions used to calculate the voltage and power output in COMSOL are also introduced in this chapter.

Chapter 5 summarizes the experimental methodology and setup used to acquire the Modal Assurance Criterion (MAC) and various frequency response functions (FRFs). Furthermore, this chapter briefly goes over the fabrication of the energy-harvesting unit, followed by the electrical wiring used to acquire power FRF.

Chapter 6 describes the procedure followed to obtain the design modeshapes from COMSOL as well as the experiments. The subsections compare the experimental modeshapes with the numerical modeshapes to evaluate the MAC number. The MAC number quantifies the coherence of these modeshapes with each other. The chapter concludes by validating the solid mechanics aspect of the numerical simulation.

Chapter 7 presents a detailed dynamic analysis of the proposed design. After validating the simulation, extensive studies are performed to study the generation of strain nodes and the natural

frequency of the design. Moreover, a similar analysis is performed for the zigzag design to show the advantages of the folded design.

Chapter 8 presents the final comparison between the fabricated unit and the numerical simulation. It starts by comparing the first three natural frequencies of the design from experiments and simulation. This is followed by the displacement comparison at the tip and the center of the design. This section briefly describes the evaluation of damping ratios using the displacement FRFs which are then accommodated in the final simulation to acquire voltage and power FRFs. The final subsection summarizes the results by confirming the validity of the numerical simulation.

Chapter 9 outlines the various comparisons made between the power densities of the proposed design with the pre-existing designs. This section uses the results obtained from the previous chapter to create a simulation for simpler geometries with confidence and use their results for power comparison.

Chapter 10 concludes the results from the previous sections and outlines the potential future steps that can be taken to further optimize this design.

Chapter 2
Literature Review

In this chapter, the principle of piezoelectric energy harvesting is explained, followed by the description of most generic piezoelectric energy harvester, a cantilever beam. The limitations of the cantilevered geometry are discussed, and low frequency energy harvesting is introduced. Furthermore, it reviews previously published designs to provide an understanding of the accomplishments and remaining drawbacks.

2.1 Piezoelectric Energy Harvesting using Ambient Vibrations

Piezoelectric energy harvesting devices that extract energy from ambient vibrations have received significant attention in the past decade due to their desirable power densities and lack of dependence on a supplemental power source [5], [8]. Other energy harvesters, such as electromagnetic and electrostatic devices, either have low voltage output or require an additional voltage source to operate, which limits their use for wireless sensors applications [8], [9]. The piezoelectric material, brittle in nature, is adhered to the substrate material, which transfers the strain to the piezo material. Due to the crystal structure of this material, the applied mechanical strain creates an electrical polarity in the material, generating an electric current. This electric charge results in a voltage output from the harvester that can charge a storage component such as a capacitor. Commonly used designs for piezoelectric-based devices employ cantilever beam geometries subjected to base excitations from an ambient source due to the presence of high strain. While this is an attractive option due to its simplicity in design, it still suffers from higher than expected natural frequencies that then require further tuning using a tip mass.

2.2 Simple Cantilever Beam Energy Harvester

A majority of the literature has focussed on modeling and optimizing cantilevered unimorph or bimorph piezoelectric energy harvesters [10]–[15]. The main reason is the simplicity in design and the presence of a closed-form solution. Figure 1 shows a vibration based energy harvester developed by Roundy *et. al* as an enabling technology for WSN. The tip mass is used to tune the natural frequency of the harvester and to increase the power output. The strain produced in the piezoelectric layers from vibrations results in a voltage output across the electrodes.
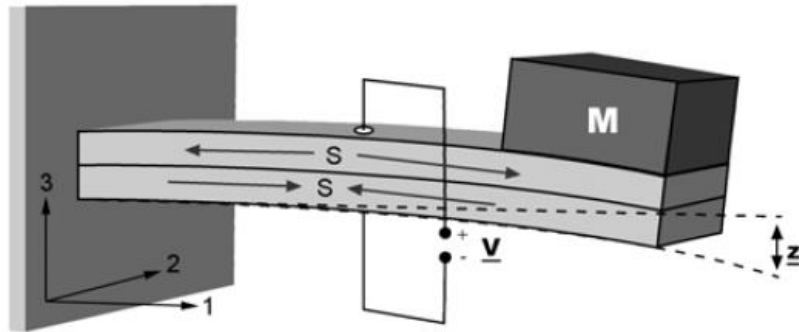
Figure 1 A two-layer cantilever beam with a tip mass. S is strain, V is voltage, M is mass, and z is vertical displacement [12]**.** *Courtesy of Roundy et al., Smart Materials and Structures (2006)*

A lumped mass model is used to model the behaviour of the harvester. A mass spring damper system represents the mechanical structure, which is coupled with the electrical circuit. Figure 2 shows the circuit coupling the mechanical and the electrical domains of the harvester to measure the power output of the system using a resistive load. The mass or inertia of the generator is represented by equivalent inductor (L_m), the mechanical damping is represented using the equivalent resistor (R_b), the equivalent capacitance (C_k) represents the mechanical stiffness and the stress developed from the input vibrations is represented using σ_{in}. The electromechanical coupling is represented using a transformer with "n" equivalent turn ratio, where C_b is the capacitance of the piezoelectric layer and V is the voltage across the piezoelectric layer.
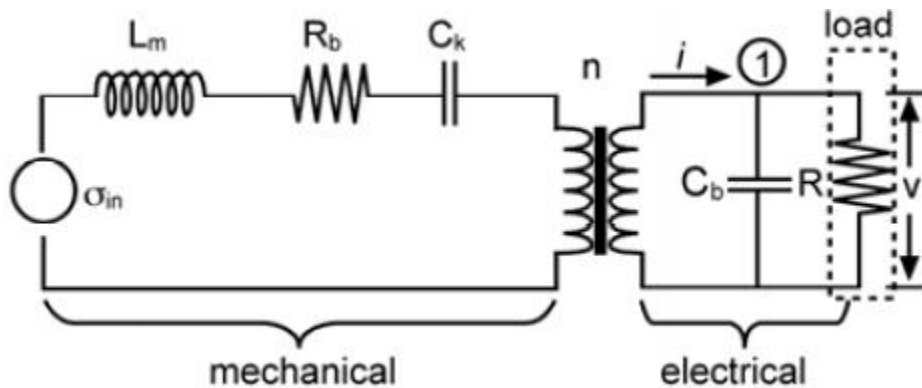
Figure 2 Circuit representation of a piezoelectric generator with a resistive load [12]**.** *Courtesy of Roundy et al., Smart Materials and Structures (2006)*

6

2.3 Low-Frequency Energy Harvesting

The recent need to decrease the size of the harvester for MEMS applications, is matched by the even more vital need to decrease the natural frequency of the harvester. For a cantilever geometry, this means a large aspect ratio or a heavy tip mass contradicting the MEMS applications due to design constraints on the size and mass of the harvester. Hence, some of the recent designs studied in the literature offer viable options for more flexible designs that keep the natural frequencies small without relying on a heavy tip mass [16]–[23]. These include techniques such as using axial loading investigated by Leland *et al.* to tune the natural frequency of the harvester, and using arc based geometry for a simple cantilever investigated by Apo et al. to further decrease the natural frequency [24], [25]. In addition to these techniques, researchers have investigated a variety of 2D geometries to increase the designs' flexibility in order to decrease the natural frequency. The upcoming subsections go over a few of the well-known designs in this area of research.

2.3.1 Zigzag Design

A zigzag design, is an interesting example of the design suggested to attain a lower frequency put forth by Karami *et al.* [16]–[18]. The idea of a cantilever beam is extended to have multiple cantilevers joined in zigzag fashion with a link. Each cantilever beam is comprised of a piezoelectric layer adhered to the substrate layer. This geometry results in an increase in the effective length of the structure without increasing the footprint, hence decreasing the frequency of the harvester. The zigzag microstructure outperforms a simple cantilever beam by producing high power density and low natural frequency.
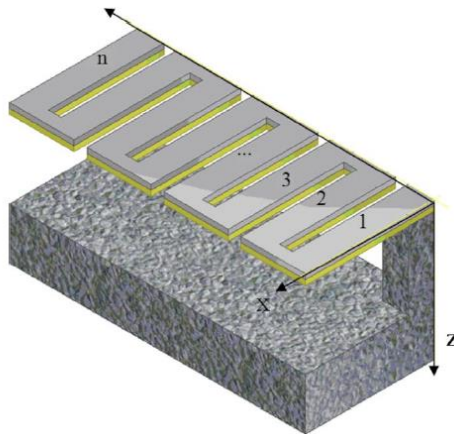
Figure 3 Energy harvester with Zigzag geometry [18]**.** *Courtesy of Karami et al., Journal of Vibration and Acoustics (2011)*

Karami *et al's* parametric study showed that as the number of legs increased, the natural frequency of the harvester decreased. However, with the increase in number of legs, the first coupled mode of vibration became increasingly torsional. This led to dominantly torsional vibrations as the number of legs increased beyond ten members [17]. Since bending vibrations are primarily used for piezoelectric energy harvesting, the increase in members will result in a lower power output.

2.3.2 Flex Configuration

After analyzing the zigzag microstructure and understanding the dominance of torsional mode, Sharpes *et al.* presented the so-called "Flex" configuration. This design focused on creating a symmetric zigzag to elevate bending mode as the primary mode of vibration which is necessary for high electromechanical coupling [26]. As shown in Figure 4, this design zigzags from the central beam in either direction making the final geometry symmetric about the clamp. The piezo material is patched at the area of concentrated stress, near the clamped end, to increase the power output.
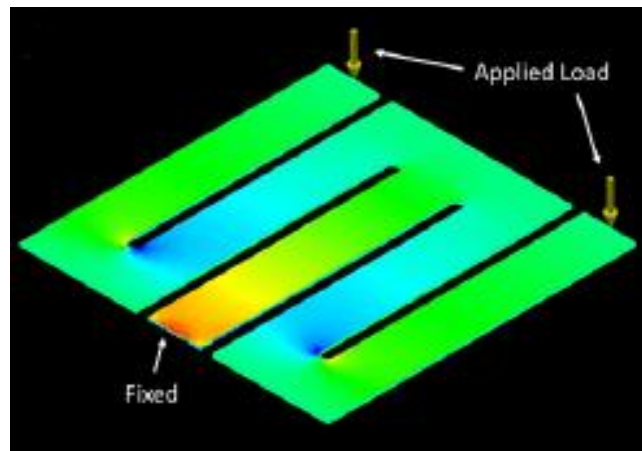
Figure 4 Flex Zigzag configuration showing the fixed and free ends [26]**.** *Courtesy of Sharpes et al., Applied Physics Letters (2015)*

This design was able to produce higher power than the zigzag design, which was followed by the "Elephant" configuration. However, as the design became symmetric, the effective length of the design decreased, resulting in a higher natural frequency than a zigzag design of same footprint.

The Flex configuration is discussed in detail rather than the Elephant configuration because this configuration is used as a benchmark for comparison with the proposed design in the later sections.

2.3.3 Quad Folded Design

In order to decrease the footprint of an energy harvester, Paprotny *et al*. investigated a quad folded design for MEMS AC energy scavenging. The geometry was designed and fabricated while making sure that the energy harvester fit within a 10x10x4 mm^3 volume. Figure 5 shows the proposed memory stick sized wireless sensor node containing the MEMS AC energy harvester. The quad folded design with 4 turns, Figure 6, of folded spring is able to achieve the desired frequency of 60 Hz. It is essential for the harvester to resonate at this natural frequency in order to maximize the power harvested from AC current.
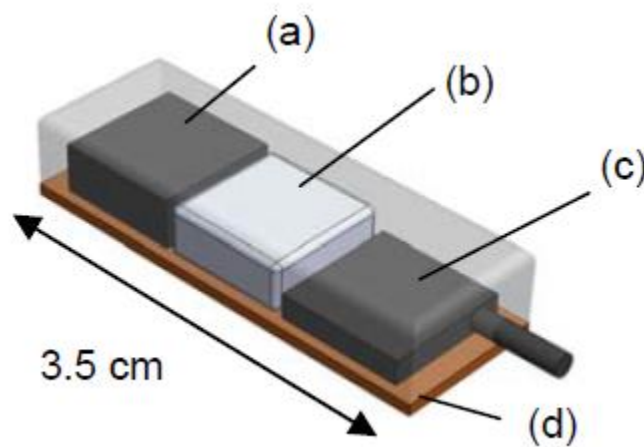
Figure 5 The proposed memory-stick sized wireless senor node containing the die sized current scavenger (a), a MEMS current sensor circuit (b), a wireless radio chip (c) and the circuit board substrate (d) [27]**.**
Courtesy of Paprotny et al., Micro Nanotechnology Power Generat. Energy Convert. Appl.

Figure 6 The quad-folded design with n=4, where "n" is the number of turns of folded spring [27]**.**
Courtesy of Paprotny et al., Micro Nanotechnology Power Generat. Energy Convert. Appl.

The energy harvester is fabricated using bulk micromachining of an SOI-wafer with 2 μm BOX layers [4]. The final design produced approximately 2 μW of power from current as low as 1 A_{RMS} while indicating a potential to scavenge higher power.

2.3.4 Spiral Design

The geometry of a long cantilever can be folded into a spiral cantilever structure to meet the size and natural frequency constraints. The dynamics of spiral geometries were studied by Brewer *et al*. to show their impacts on their natural frequencies [28]. The dependence of spiral beams' natural frequencies on width was also studied. A spiral geometry was also investigated by Ibrahim *et al*. for hybrid energy harvesting employing the use of piezoelectric, magnetostrictive and electromagnetic technologies [29]. Figure 7 shows the FEA model of the spiral beam geometry used to analyze the dynamics and the power output of the spiral design.
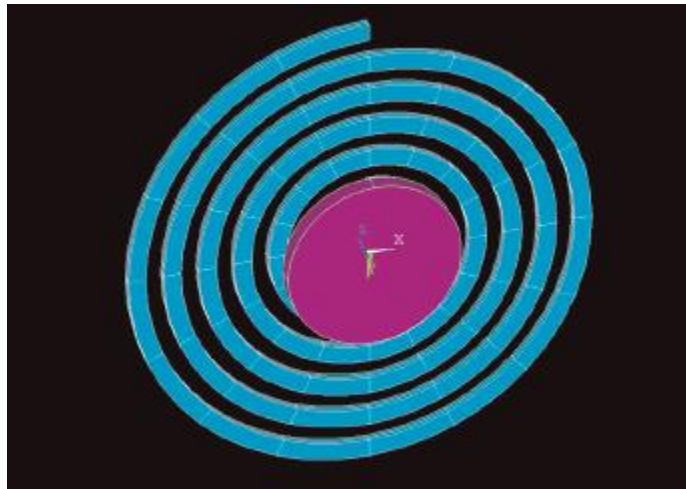
Figure 7 Piezomagnet harvester containing a spiral piezoelectric bimorph and a magnet attached to the center of the spiral [29]**.** *Courtesy of Ibrahim et al., Journal of Intelligent Material Systems and Structures (2015)*

This geometry was further studied by Karami *et al.,* who showed that the vibrations of the spiral are mostly torsional in nature, hence complicating the use of this geometry for vibration energy harvesting applications [20]. Therefore, even though this geometry is successful in decreasing the natural frequency while having a low aspect ratio, the presence of torsion in the main mode of vibrations cause limitations on its use as an energy harvester.

2.3.5 Meandering Design

In addition to the previously described geometries, various meandering designs have also been researched to decrease the natural frequency and increase the power output. The meandering geometry shown in Figure 8 is symmetric about the free end of the harvester. It is also evident from this figure that the strain changes its direction in consecutive legs. In other words, if the strain is positive for one leg, then it is negative for the legs that are immediately next to it. Therefore, strain nodes are found at each beam connection in this geometry. Strain nodes, as defined by Erturk *et al.*, are the positions where the strain switches directions for a given vibrational mode [30]. Avoiding strain nodes is essential in energy harvesters because covering the area in close proximity of a strain node with continuous electrode results in charge cancellation from the piezoelectric layer. This is particularly important for smaller aspect ratios, as when the leg length becomes smaller than the width, torsion tends to become the dominant fundamental mode. Hence, covering the entire harvester with one continuous electrode will result in charge cancellation, causing a diminished voltage output.
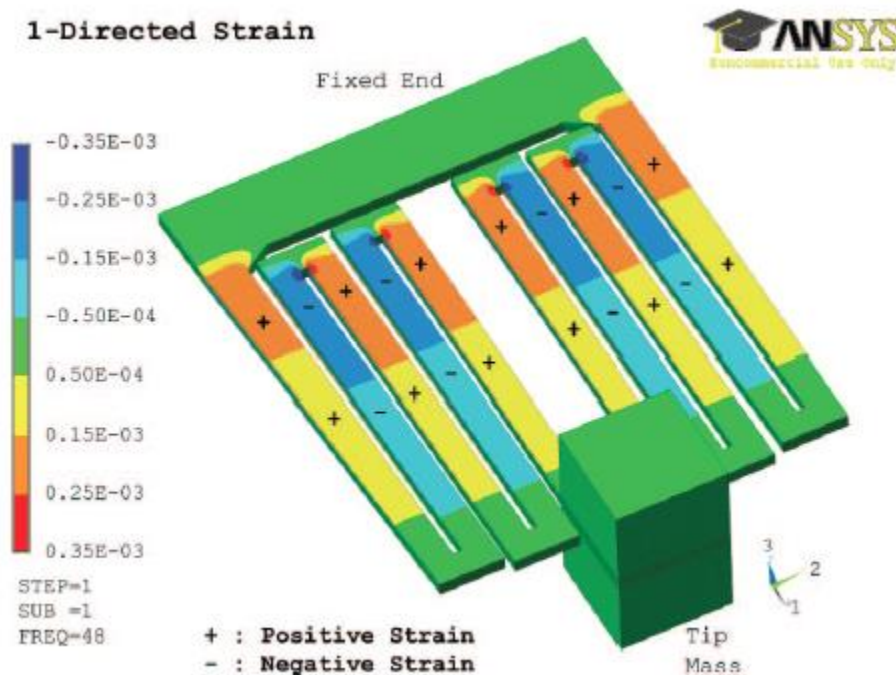
Figure 8 Meandering geometry showing strain contour along the top piezoelectric layer [19]**.** *Courtesy of Berdy et al., IEEE transactions on Ultrasonics, Ferroelectrics, and Frequency Control (2012)*

11

Different techniques such as Strain-Matched electrode (SME) and Strain-Matched Polarization (SMP) can be used to avoid the voltage cancellation [19]. Two different electrodes, one covering the positive strains and the other covering the negative strains, are used in the Strain-Matched electrode technique. Figure 9-(a) shows the strain matching of electrodes, which are electrically isolated at the strain nodes. With the strain-matched polarization technique, only one electrode is used, and instead, the piezoelectric strip itself is polarized based on the strain. Hence, if the positive strain is matched with the strip that is polarized in the positive 3 direction, then the negative strain is matched with the strip polarized in the negative 3 direction. This method requires much simpler wiring than to the SME design due to the presence of one continuous electrode.
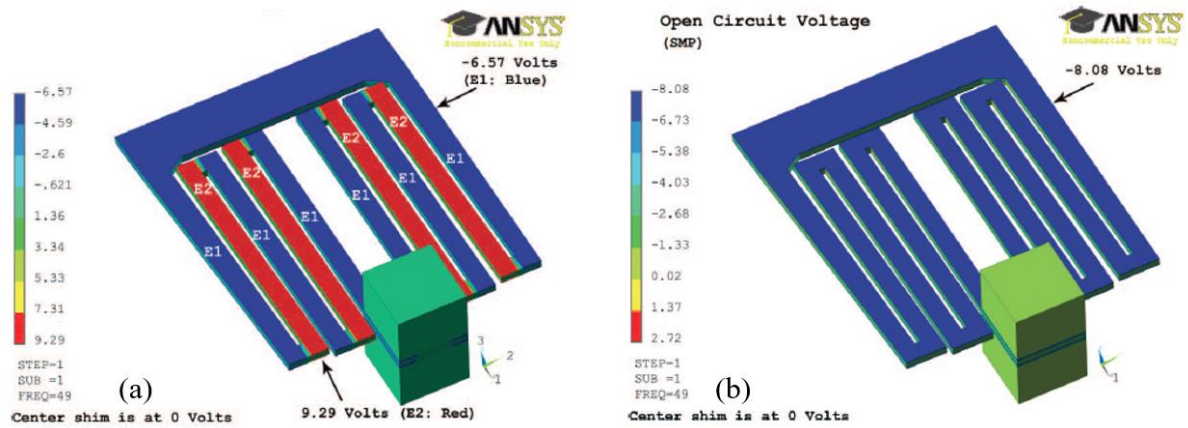
Figure 9 Simulated open-circuit voltage for the meandering (a) strain-matched electrode design and (b) strain-matched polarization design [19]. *Courtesy of Berdy et al., IEEE transactions on Ultrasonics, Ferroelectrics, and Frequency Control (2012)*

It is evident from the results that the SME and SMP techniques produce a higher voltage than the design with a single electrode without any strain matching polarization. In addition, the SMP method produces slighly higher voltage than the SME design due to the reduced damping from simpler wiring connections. Hence going forward, the SMP method is used to fabricate the proposed design based on the results shown by Berdy *et al.*

Chapter 3
Design Geometry

In this chapter, the criteria and constraints used to design the harvester's geometry are discussed in detail. The initially proposed design is also shown along with its advantages and drawbacks over previous geometries. Strain nodes contours from the respective COMSOL simulations are plotted to show the presence of strain nodes on different geometries. Lastly, the final design is presented, and its advantages over previous designs are discussed.

3.1 Criteria and Constraints

Before proposing a new design for an energy harvester, some criteria and constraints are developed to focus on the major drawbacks of the existing designs. As described in the previous chapter, this research has attracted significant attention in the past decade, and researchers have proposed numerous geometries. However, there is still a need for a design that can reduce the existing designs' natural frequencies even more while increasing its power density. Hence, the proposed design should have a lower natural frequency than the previously designed geometries while producing a higher power density. In addition, the ease of fabrication, low manufacturing cost, and variability in design for different applications are additional criteria.

3.2 Initial Design

The major motivation for the proposed design comes from the state-of-the-art zigzag design studied by Karami *et al,* which produced much lower frequencies than its 1D counterpart i.e. the cantilever beam. By introducing another dimension to the geometry and making the design 2D, Karami lowered the natural frequency, which also resulted in an increased power output. In order to reduce the frequency low enough (<100 Hz) to harvest energy off of ambient vibrations, the design must have a greater number of beams. While this was an attractive approach, the increase in the number of members resulted in a torsional mode being the fundamental mode of vibration. Since energy harvesters use the bending mode to produce higher power, this was considered as a potential drawback for this design. The proposed initial design came forth in an attempt to decrease the natural frequency of the zigzag design for the same footprint. This resulted in zigzagging the design in all three dimensions as shown in Figure 10. By introducing the third dimension, the effective length of the design can be increased

while keeping the same footprint. This results in a lower natural frequency than its 2D counterpart i.e. the zigzag design.
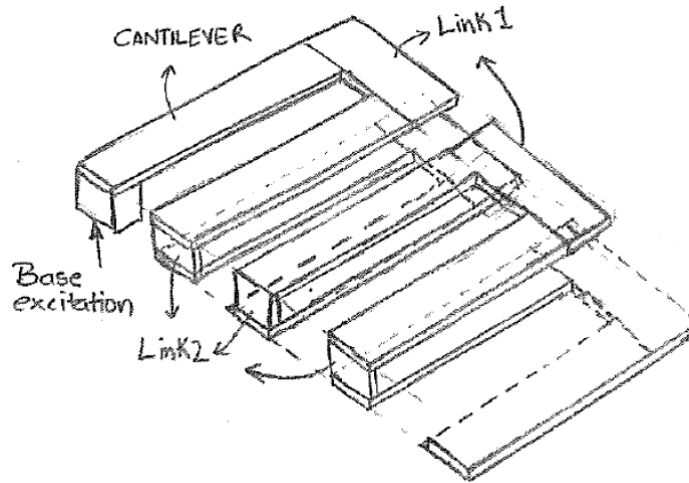
Figure 10 Initial sketch of the overlapped length zigzag design

A COMSOL simulation was created for this design to analyze the dynamic behaviour of the design and to evaluate its natural frequency. Chapter 4 explains in detail the COMSOL simulations and studies used to plot the strain profiles. With a lower natural frequency than the zigzag, this design appeared more promising for MEMS applications. Following the same strain contour (Figure 11), as the zigzag, this design was well on its way to be the next leading design in the energy harvesting community.
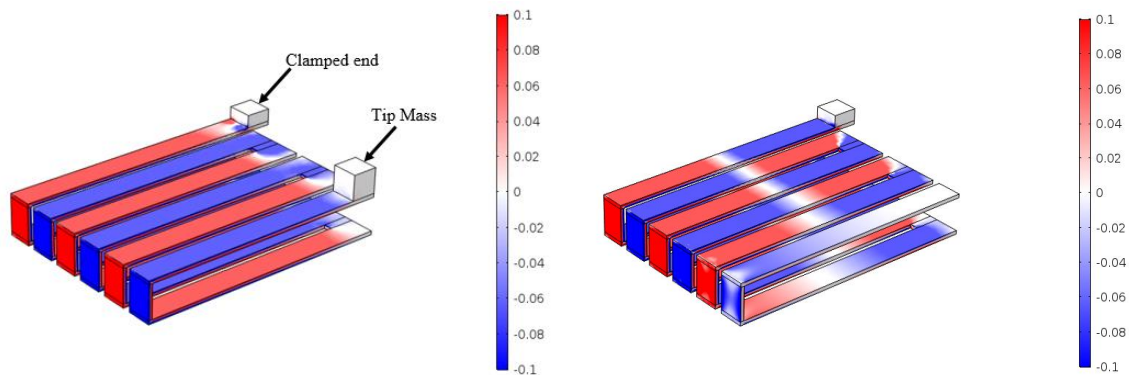
Figure 11 Overlapped length zigzag design with tip mass (left) and without (tip mass) showing strain contour

However, the zigzag design proposed by Karami *et. al* showed the presence of strain nodes for the fundamental mode. Figure 12-a shows the zigzag design with five legs having strain nodes in the middle of its legs due to presence of torsion. Similar behaviour was noted (Figure 11) for the overlapped length

14

zigzag design when the tip mas was removed. In order to avoid the strain nodes, a second version of this design was created.

3.3 Final Design

The motivation behind the final design came from the flex configuration proposed by Sharpes *et. al*. Their study shows that, as the design becomes more symmetric (Figure 12-b) the fundamental mode switches from a coupled mode (bending-torsion) to a pure-bending mode, thus increasing the electromechanical coupling [26]. As the primary mode of vibration becomes dominantly bending, the strain nodes disappear. This idea of symmetricity is used to design the final geometry proposed in this paper. Hence, the symmetric zigzag design is folded on itself to create a 3D design for an energy harvester. This final design is named the "Folded Zigzag", and Figure 12-c shows the strain plot of this design for the fundamental mode of vibration. Similar to the flex configuration, the folded design results in bending becoming the dominant fundamental mode, hence reducing the torsional effects for this mode. Consequently, the design has fewer strain nodes, which aids with the electrode geometry.

It should be noted that, as the design becomes symmetric, end clamp to center clamp, the effective length from the clamped end to the tips decreases. This results in an increase in the natural frequency of the design. The natural frequencies for the first mode of vibration for all three designs having the same footprint are shown in Figure 12's caption. The proposed 3D folded design, Figure 12-c, has a larger clamp to tip distance than the flex configuration while having the same footprint, and therefore the behaviour of the natural frequency and power output is of interest. This paper shows that the additional flexibility provided by the zigzag pattern in both planar and vertical directions results in better flexibility over similar footprints of single story, planar geometry. This is always an advantage for vibrational energy harvesting applications given the generally low frequencies, less than 100 Hz, available through an ambient source [7]. Additionally, the proposed design allows for fewer strain nodes due to its design and symmetricity for the clamp location compared to planar symmetric zigzag design.
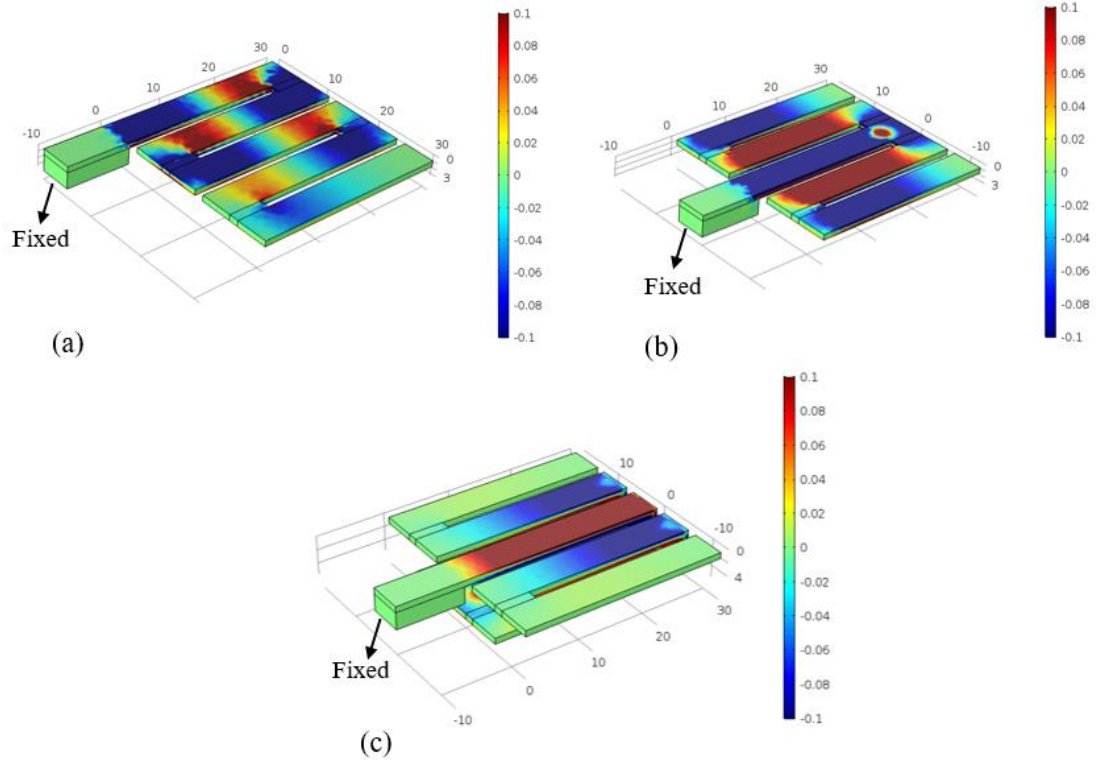
Figure 12 Strain plots for fundamental frequency of (a) zigzag (148 Hz) (b) planar symmetric zigzag (299 Hz) and (c) folded 3-D zigzag (160 Hz). Coloring of all the above screen shots is in reference to the strain scale shown (mm/mm). The approximate dimensions shown by the grid are in mm. The rectangular block represents the fixed/clamped end of each design.

Chapter 4
Numerical Setup

This chapter presents the design and modelling of the proposed energy harvester. The steps taken to model the substrate and the PZT along with their material properties are described in detail. Different COMSOL modules used to analyze the dynamic behaviour and piezoelectric affect are also discussed in this chapter.

4.1 COMSOL Multiphysics

The Multiphysics module of COMSOL is used to create a numerical simulation of the proposed folded zigzag energy harvester. This module couples different domains of physics to study their effects on each other. In order to analyze this design, the Solid Mechanics module is coupled with the Piezoelectric effect, Electrostatics and Electric circuit modules. The Eigenfrequency analysis is used to obtain the natural frequencies and strain plots of the proposed design. Once the resonant frequency is evaluated, the Frequency-Domain study is performed about the resonant frequency range. This study performs the FEA analysis on the design for each frequency, which is then used to produce numerous FRF plots.

4.2 Geometry, Substrate Modeling and Boundary Conditions

The 3D model of this design is primarily created in SolidWorks and imported to COMSOL for Finite Element Analysis (FEA). Table 1 below shows the geometric dimensions used to create the harvester in COMSOL. The sheet metal feature of SolidWorks is used to create the two 90° bends in order to fold the design on itself. Figure 13 shows the final dimensions of the substrate and the PZT that are used for the numerical simulation.

Table 1 Geometric dimensions for the design and the peizo strips

Property	Folded Zigzag
Length of each member (mm)	30
Width of each member (mm)	5
Thickness of substrate (mm)	0.88
Distance between consecutive members (mm)	1.5
Distance between the top and bottom layer (mm)	4
Number of Legs	5+3
Length of piezo strip (mm)	20
Width of piezo strip (mm)	5
Thickness of piezo strips (mm)	0.191

Mass of individual cylindrical magnet (g)	1.5
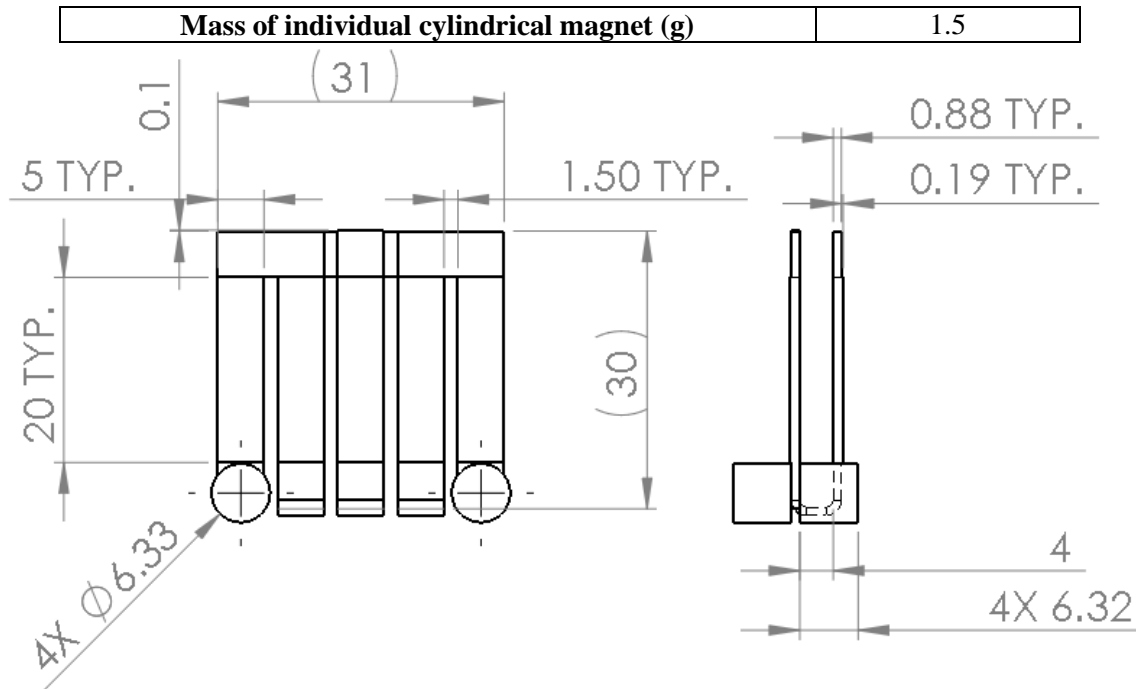
Figure 13 Schematic showing the dimensions (in mm) of the substrate as well as the PZT for the Folded zigzag design

A block is used to represent the clamp, and the "Fixed constraint" boundary condition is used as shown in Figure 14. The domain of the block was given a prescribed acceleration of "g_const*acc" in the z-direction to replicate the base excitation from the electrodynamic shaker. Here, g_const is the gravitational constant with a value of 9.81 m/s^2, and acc is the constant multiplier. Two cylindrical protrusions represent the magnets used on both the free ends of the harvester as tip masses. The substrate material is selected as the linear elastic material while the piezo strips are selected in the piezoelectric material subsection.
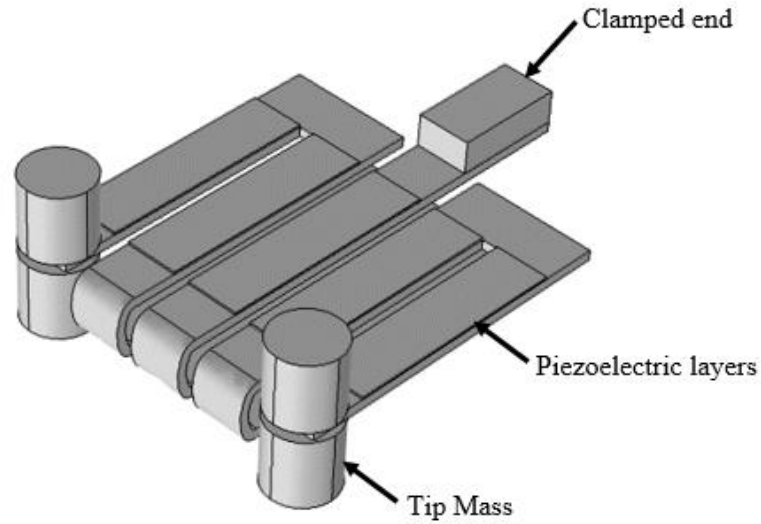
Figure 14 COMSOL model of the piezoelectric energy harvester

4.3 Piezoelectric Modeling

The piezoelectric material used for this energy harvester is poled in the z-axis and is strategically adhered to each leg depending on the direction of strain. Poling is the process of subjecting the material to a very high electric field to align the dipoles of the material in the direction of field. In order to ease the fabrication and the experimental setup, the piezo strips are placed on the top of the top layer and bottom of the bottom layer. With the piezoelectric material poled in the z-axis, the strain-charge form of piezoelectric constitutive equations can be applied:

$$S_1 = c_{11}^E T_1 + d_{31} E_3 \qquad (1)$$

$$D_3 = d_{13} T_1 + \epsilon_{33}^T E_3 \qquad (2)$$

where D is the electric displacement, E is the electric field, S is strain, T is stress, c^E is the compliance with constant electric field, d is the piezoelectric coefficient, and ϵ^T is the permittivity under constant stress.

In order to strain match the electrodes, the electrostatic module is used to wire the tensile strains to the terminal electrode and the compressive strains to the ground electrode. The SME process is used in COMSOL instead of SMP as all the strips are polarized in one direction. The PZT strips for the top and bottom layers were wired using the SME process as shown in Figure 15.
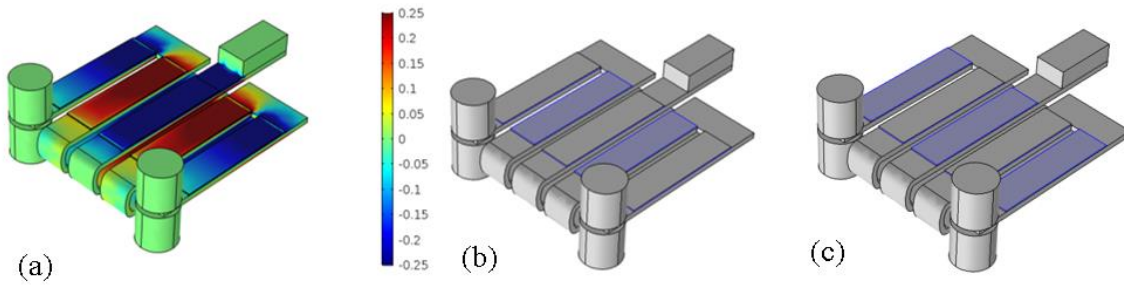
Figure 15 Schematic showing (a) Strain contour using eigenfrequency analysis for fundamental mode, (b) the ground electrode connections and (c) the terminal electrode connections

4.4 Material Properties and Meshing

In order to keep a low natural frequency and high power density, attention must be paid to the materials used for the substrate and the piezo strips. The purpose of the substrate material is to support the PZT strips while adding as little stiffness to the design as possible. To meet this requirement, a substrate material with a low Young's modulus should be selected to maintain the design's flexibility and achieve a low natural frequency. In addition, to keep the wiring simple and to use the substrate as the ground electrode in the circuit, the substrate needs to be conductive. Therefore, stainless steel, being cheaper and more durable (Table 2), is chosen as the substrate since it complies with all the above requirements and is readily available.

Table 2 Stainless Steel material properties

Young's Modulus	190 GPa
Density	8000 kg/m^3
Poisson's ratio	0.24

It is also necessary to select a piezoelectric material with high electromechanical coefficient to produce maximum power. Additionally, the piezo material must be suitable for the fabrication and experimental process. With this in mind, Lead Zirconate Titanate (PZT) is used as the piezo material due to its high electromechanical coefficient and availability of custom manufacturing to meet the design specifications. The energy harvester is fabricated using the Navy Type II PZT, also called PSI-5A4E from Piezo Systems. Figure 16, 17 and 18 show the compliance, coupling and relative permittivity matrices provided by the manufacturer for the PZT used respectively.
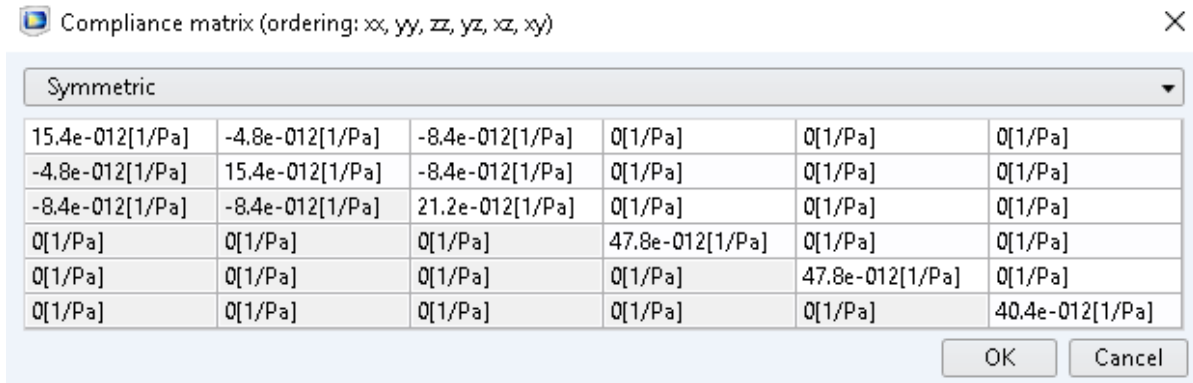
Figure 16 Compliance matrix for PSI-5A4E
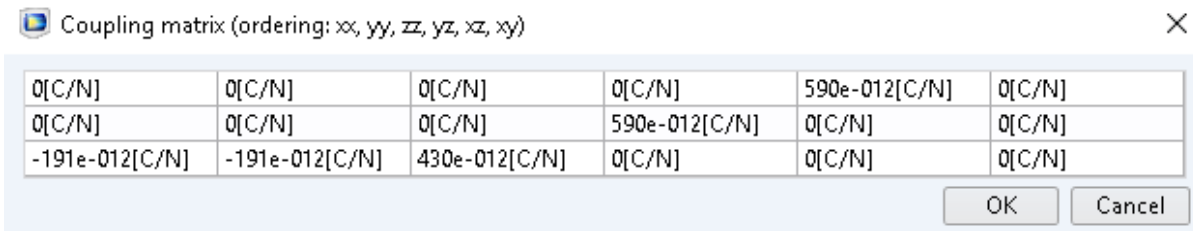
Figure 17 Coupling matrix for PSI-5A4E
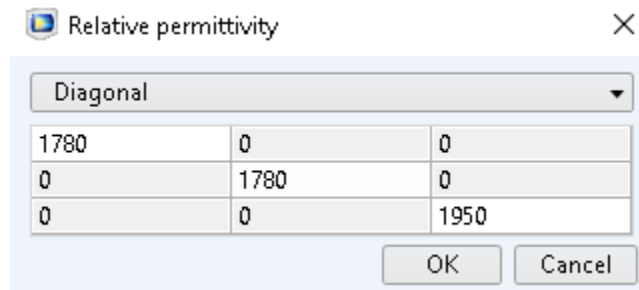
Figure 18 Relative permittivity matrix for PSI-5A4E

The COMSOL software has inbuilt default levels for meshing that are controlled by the type of physics module being used. The mesh used for this design was created using the predefined "finer" free tetrahedral elements, which resulted in an incremental change of less than 1 % for eigenfrequencies.

Table 3 Numerical Simulation Meshing Information

Number of Elements	213858
Mesh Vertices	46683
Edge Elements	4316
Average Element Quality	0.7

4.5 Voltage and Power Output

The end-goal of the frequency-domain analysis is to plot the voltage and power FRF's for the energy harvester. In order to do so, the formulas shown in Figure 19 and Figure 20 are used to evaluate the voltage and power produced by the design at each frequency. Both the voltage and power are calculated as root mean square (RMS) values to make the final comparison with the RMS data from the experiments.

Expression	Unit	Description
abs(cir.R1_v)/(1.41)	V	Voltage (V)

Figure 19 Expression to evaluate voltage in COMSOL

Expression	Unit	Description
0.5*realdot(cir.R1_i,cir.R1_v)	W	Power (W)

Figure 20 Expression to evaluate power in COMSOL

The "cir.R1_v" represents the voltage across resistance 1 in the circuit, which is the external resistance in this case. The power is evaluated by multiplying the voltage across resistance 1 with the current, "cir.R1_i".

Chapter 5
Experimental Setup

This chapter presents the experimental setup used to gather the modeshape and power output data. These experiments are used to validate the numerical model and establish confidence in the results from the studies in Chapter 6, 7 and 8. In addition, the fabrication of the energy harvester using the SMP technique is presented. Finally, the electrical connections used to evaluate the voltage and power outputs are briefly discussed.

5.1 General Setup

Experiments are performed in order to establish confidence in the simulation as a tool for varying several system parameters. An LMS SCADAS module, model SCM 05, was used to acquire the experimental results for each design in order to validate the findings from COMSOL [31]. The units were clamped to the dual-purpose electrodynamic shaker (Modal Shop, model 2075E [32]) which provided the required base excitation as shown in Figure 21. The shaker was controlled by the LMS mobile data acquisition system through a laptop containing the LMS test lab software. The laptop was connected to the LMS module to control the output signals and to perform real time measurement of displacement, voltage and power. The PCB accelerometer, model 352A24 [33], was used as a feedback loop to control the base acceleration over the given range of frequencies. The accelerometer used had a sensitivity of 100.9 mV/g, and was able to operate up to 10,000 Hz.

The displacement of the unit was measured using a laser vibrometer with a Polytec OFV 505 sensor head and an OFV-5000 controlling unit made by Polytech [34]. The displacement was recorded by taking advantage of the Doppler Effect and measuring the frequency shift of the reflected laser beam of light. The laser beam was physically moved to the various sensing locations to measure the displacement at multiple points, which was then used to evaluate the mode shapes. The voltage and power FRFs were acquired by connecting the BNC crocodile clamps across a variable resistor box to measure the output voltage. The LMS Sine Sweep module was used to transform the sinusoidal signals produced by the harvester into an RMS voltage FRF.

The experimental setup was the same for the two experiments performed in this paper. The validation of the solid mechanics part of the simulation was done by evaluating the MAC number between the experimental and numerical modeshapes; this comprises the first set of experiments. During these

experiments, only the displacement was plotted for numerous points to plot the operational deflection shape.

On the other hand, the validation of the entire simulation (i.e. the solid mechanics, electrostatics and electric circuit module) was done by plotting the voltage and power FRFs between the experimental and simulation results, which is the second set of experiments.
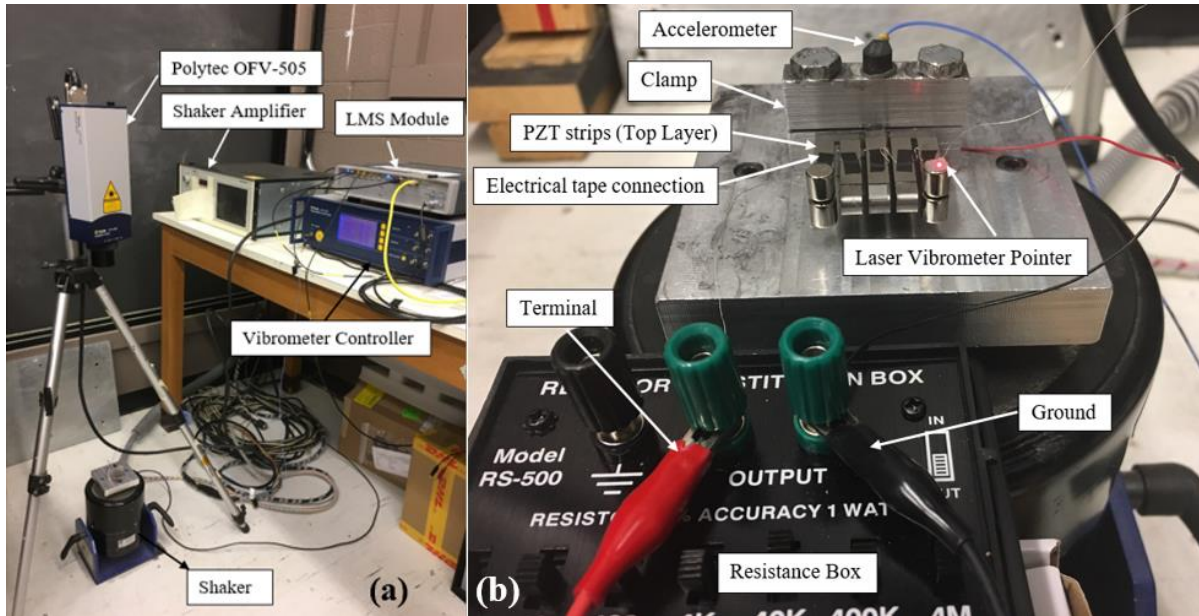
Figure 21 Experimental test setup showing (a) the laser, shaker and LMS setup (b) the clamped test unit along with the accelerometer and the wiring

5.2 Design Fabrication

The fabrication of this design took place in the vibrations lab at the University of Waterloo campus. KJ micromachining services are used to laser cut the flat pattern of the proposed design, and a material forming process is used to bend the flat pattern into shape [35].

This section covers the systematic fabrication for the energy harvester. As shown in Figure 22-a, the PZT strip is marked with a horizontal line to define the poling direction. The PZT is poled in the thickness direction pointing out of page. In order to use the substrate as the ground connection for wiring, silver epoxy is used to maintain the electrical conductivity between the PZT and the substrate. The silver epoxy paste is created by mixing the resin and hardener from Atom Adhesives in 1:1 ratio (Figure 22-b). Once the resin is thoroughly mixed with the hardener, it is applied to the side of PZT that is being adhered to the substrate as shown in Figure 22-c and 22-d. Uniform pressure is applied to

the PZT strip in order to fill any voids while removing any additional overflow from the sides. The setup is left untouched for 24 hours for the epoxy to dry before performing any tests (Figure 22-e).
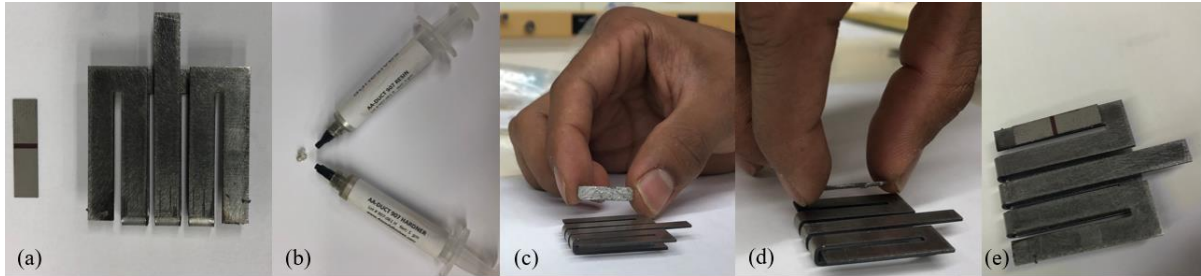
Figure 22 Fabrication of harvester showing (a) the harvester and PZT strip, (b) Silver epoxy used for adhering the strip, (c) PZT strip with silver epoxy, (d) Adhering PZT onto the harvester and (d) Harvester with PZT

The same procedure is followed to adhere all the PZT strips on top of the top layer and bottom of the bottom layer of the unit. SMP is used to avoid any voltage cancellations by adhering the PZT poled in positive direction to tensile strain and the negative direction to the compressive strain. In Figure 15-a, the strain alternates among the legs of the harvester, which results in alternating PZT strips polarized in opposite directions as shown in Figure 23.

Figure 23 Manufactured unit showing the polarization of PZT strips along with the top and bottom isometric view

5.3 Electrical Setup

The use of SMP technique while fabricating the design simplifies the required electrical setup. Using this technique, the substrate can be used as the ground connection, and the top of the PZT strips can be used as the terminal. This is represented using a circuit diagram in Figure 24, which shows the top layer piezoelectric strips being wired in series with each other, and parallel to the external load. In this circuit, the current source depicts the current coming from the PZT strips, the capacitor represents the PZT

25

itself along with its internal resistance, namely Rp, and the load resistance and voltage are represented by R_l and Vp respectively. This circuit would be much more complex if the PZT strips were not strain matched in the manufacturing phase.
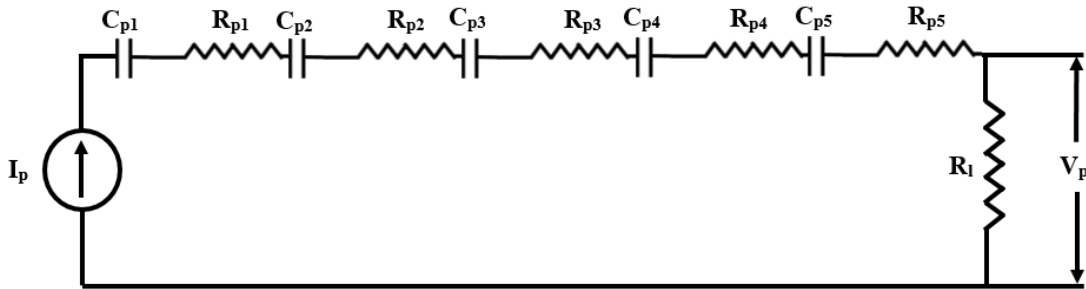
Figure 24 Electrical circuit representing the parallel connection between the PZT-strips and the resistor for top layer

Figure 25 shows the wiring of the manufactured unit, where the silver wire connects the top of each PZT strip and the red wire is connected to the substrate. These wires are then connected in parallel with the resistor box to apply an external load, across which the voltage and power are measured. Black electrical tape is used to create temporary connections between the wire and the strips.
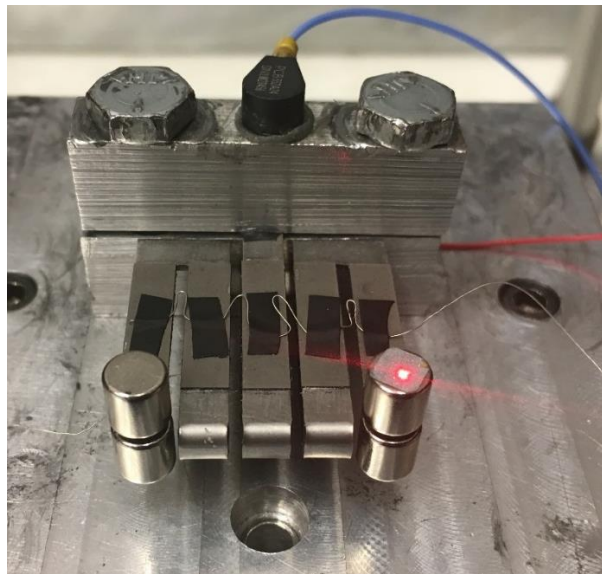
Figure 25 Electrical connections for the top layer

Chapter 6

Modeshape Validation

This chapter validates the solid mechanics module of the numerical simulation by presenting the modal Assurance Criterion (MAC) evaluation of the experimental and simulation modeshapes. It also compares the displacement FRFs from the simulation and the experiments at different positions. Finally, it presents the first three modeshapes of both the folded and planar symmetric zigzag design from COMSOL as well as the experiment.

6.1 Purpose

In order to investigate the advantages of the folded over the planar symmetric zigzag design, first the simulations for both the geometries need to be validated. Once validated, the simulations can be carried out for various parameters to quantify the dynamic behaviour of the designs. The criteria used to validate the simulation include the displacement FRFs, the structural modeshapes, and the MAC value.

6.2 Experimental and Simulation Results

In this analysis, only the dynamics of the substrate are validated, which means there are no PZT strips on the design. The COMSOL simulations are created for both the folded and the planar symmetric design using the substrate dimensions in Table 1. Figure 26 is the schematic showing the tabulated dimensions of the units being experimentally analyzed. For a fair comparison, all of the system parameters are kept the same between the two units with an exception of the number of stories; it has to be different since one is a folded design with two stories and the other is planar. The first story of the folded unit has 5 legs, similar to what is used in the one story planar unit, while the additional story in the folded zigzag design has 3 legs. The same system parameters are used in the COMSOL simulations.
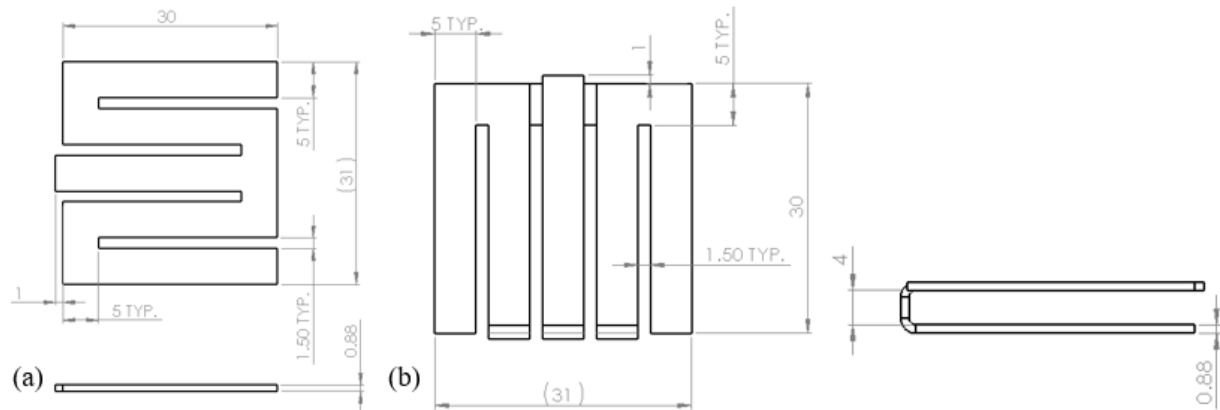
Figure 26 Top and side view of (a) planar symmetric zigzag (b) folded zigzag models used for experimental analysis with dimensions in mm.

As the parameters used in this section are primarily used for the purpose of experimental validations, a larger footprint and thickness are used to enhance durability and to prevent permanent deformation of the physical model. In the next chapter pertaining to the simulation and dynamic parametric studies, analysis on smaller scales is performed.

Multiple sensing locations are used to quantify the dynamic behaviour of the substrate to experimentally validate the numerical modeshapes. These locations are marked on the physical model in blue, Figure 27 and 28, and the displacement data is acquired at each point by physically moving the laser vibrometer. The same sensing points are also created in the LMS geometry module, and the surface feature is used to create surfaces between the points for visual representation of the modeshapes. The displacements plots are attached to the LMS geometry by selecting the particular point in LMS prior to moving the laser vibrometer and running a freuqncy-domain analysis on it. Each point on the physical model is attached to its representation in LMS for modeshape visualization purposes.
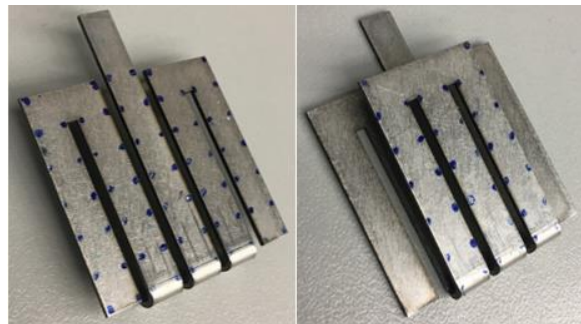
Figure 27 Folded zigzag design top (left), and bottom (right) with marked 104 sensing locations

28
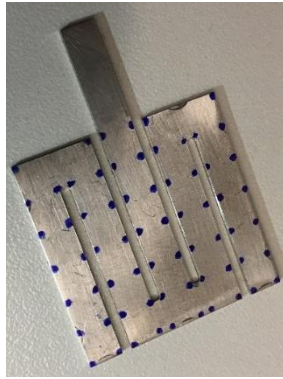
Figure 28 Planar symmetric zigzag design with marked 66 sensing locations

The displacement comparison for both of the designs is presented at two different locations to show the agreement between the experimental and simulation FRFs. Figure 29-a and b show the displacement comparison for the folded zigzag design at the center and the right tip respectively. The displacement comparison for the planar symmetric zigzag is shown in Figure 30-a and b for the center and right tip respectively.

(a)

(b)
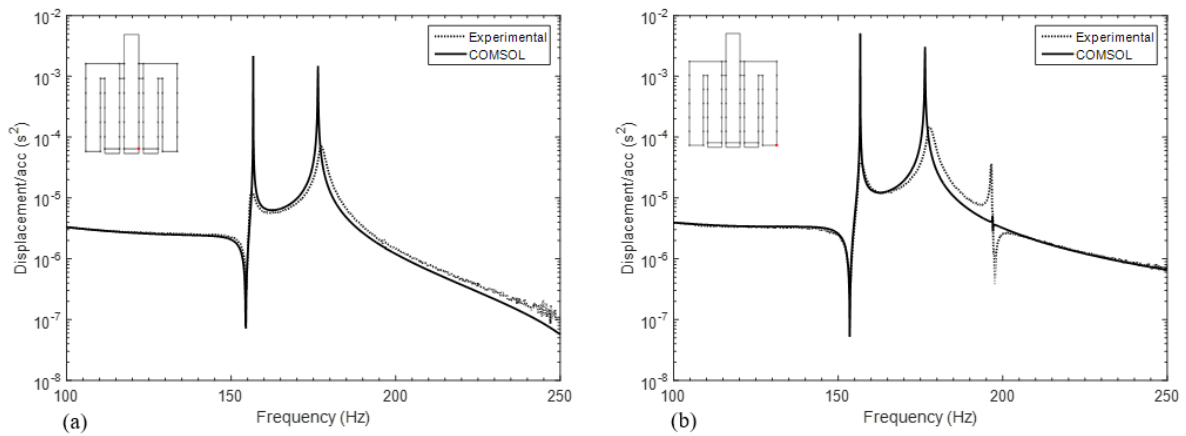
Figure 29 Displacement comparison for folded zigzag design between experiment and undamped simulation for (2) center location (b) the right tip as shown with the red dot in the illustrated figure
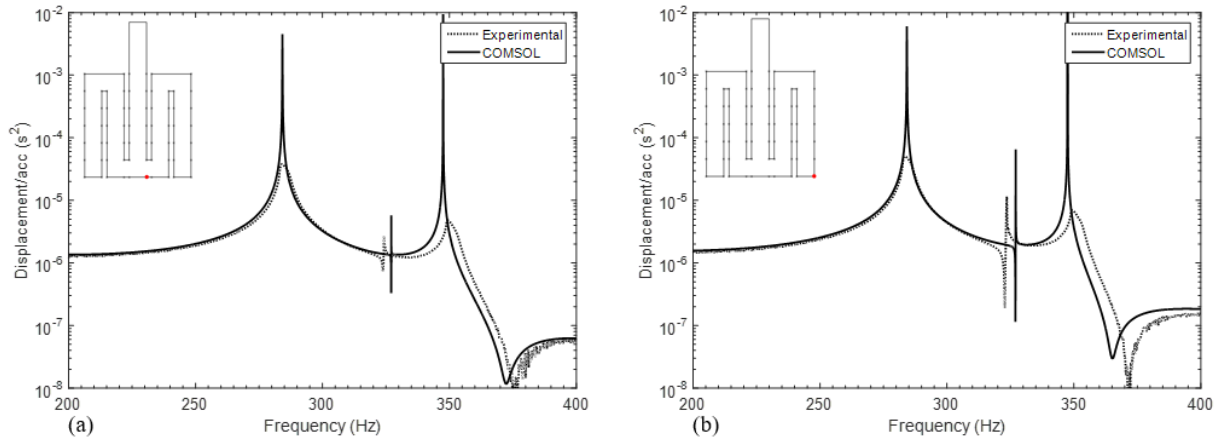
Figure 30 Displacement comparison for planar symmetric zigzag design between experiment and undamped simulation for (2) center location (b) the right tip as shown with the red dot in the illustrated figure

In order to show the effect of folding the design on itself, the experimental FRFs for the tips are overlaid in Figure 31 for both designs. It is evident in Figure 31 that the fundamental frequency for the folded zigzag unit is significantly lower for the given footprint than the planar zigzag unit (by 44% approximately).The simulation plots are performed without any damping to show the peak for the torsional mode for both the designs, as it is very sensitive to damping. Figure 31 also verifies that the torsional mode appears as the third mode for the folded design compared to the second in the planar symmetric zigzag geometry. This is a significant advantage as the torsional modes result in a larger number of strain nodes for the system,which means the electrode layouts would have to become discontinous along the members to avoid the charge cancellation. Delaying the torsional modes to the higher modes will reduce their impact on the fundamental mode, which is of primary use for harvesting applications. It is also worth noting that the folded zigzag design has a much narrower band incorporating the first two bending natural frequencies, making it more suitable for wideband energy harvesting applications than the planar symmetric design, which would not be effective over the same bandwidth.
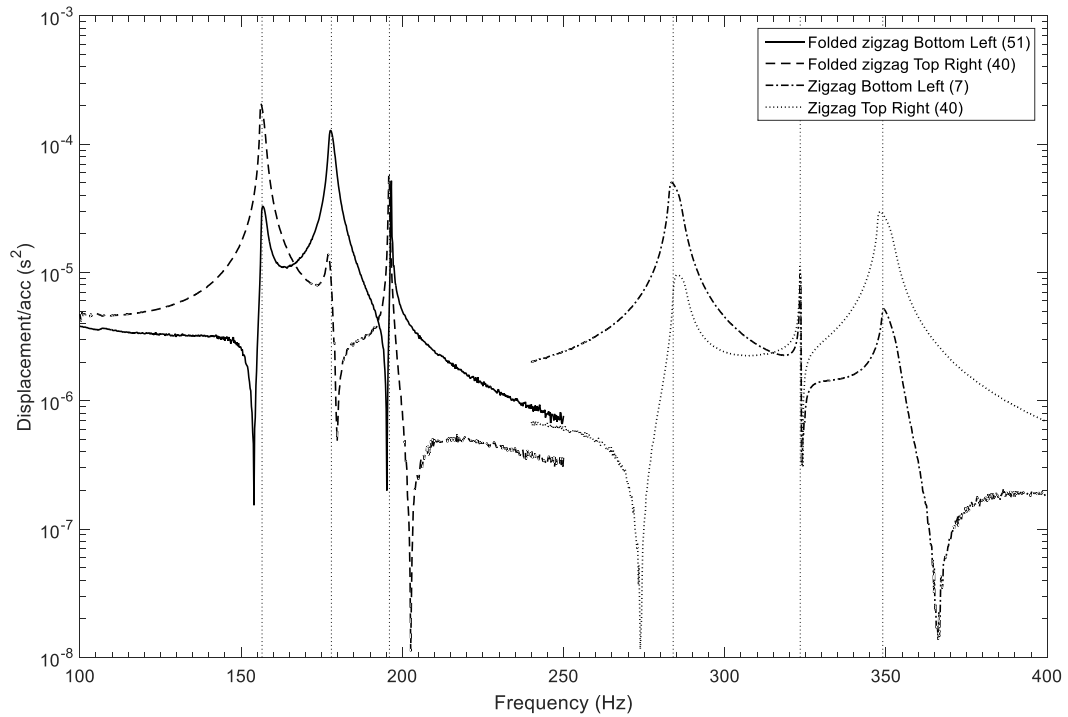
Figure 31 Experimental FRF comparison showing a lower fundamental natural frequency and higher displacement for folded zigzag design compared to planar symmetric design

6.3 Modeshape Analysis

The first three modeshapes of the folded zigzag and the planar symmetric zigzag are experimentally obtained using a SCADAS LMS module. The MAC value is evaluated in the analysis of the experimental and COMSOL simulated modeshapes for each unit to examine the coherence between the modes and to validate the COMSOL results.

Figure 32 and 33 show the COMSOL and experimental modeshape results for the planar symmetric zigzag geometry. The modeshapes from the simulation and experiment for the folded zigzag design are shown in Figure 34 and 35.

31
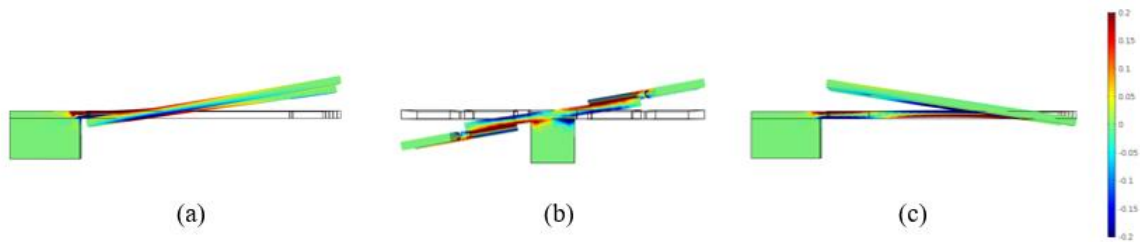
Figure 32 COMSOL modeshape plots for the first (a), second (b) and third (c) mode showing their exaggerated positions for planar symmetric zigzag design. Part (a) and (c) show the side view of the design and part (b) shows the front view
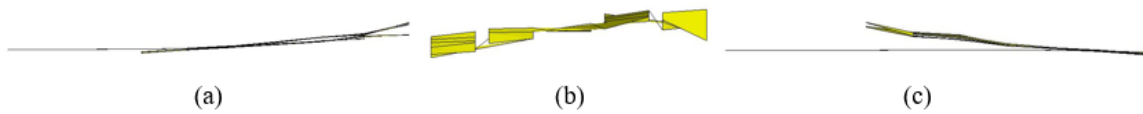
Figure 33 Experimental modeshape plots for the first (a), second (b) and third (c) mode showing their exaggerated positions for planar symmetric zigzag design. Part (a) and (c) show the side view of the design and part (b) shows the front view
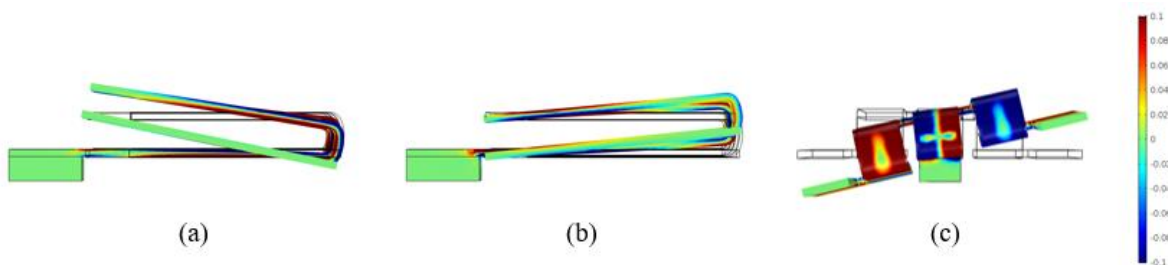
Figure 34 COMSOL modeshape plots for the first (a), second (b) and third (c) mode showing their exaggerated positions for folded zigzag design. Part (a) and (b) show the side view of the design and part (c) shows the front view
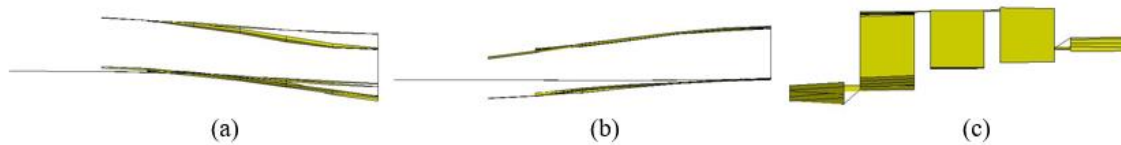
Figure 35 Experimental modeshape plots for the first (a), second (b) and third (c) mode showing their exaggerated positions for folded zigzag design. Part (a) and (b) show the side view of the design and part (c) shows the front view

The modeshapes shown in the simulation results, Figure 32, additionally confirm the previous finding from the experiments that the torsional mode appears as the second mode for the planar symmetric zigzag whereas this mode is further delayed, Figure 34, to the third mode for the folded zigzag design.

6.4 Modal Assurance Criterion Evaluation

Equation 3 is used for the MAC calculations [36], where φ_E is the experimental modeshape and φ_S is the simulation modeshape. The modeshape in this case is simply a vector assigning the displacement of each of the analysed points on the unit to an entry in the vector. The subscripts r and q represent the mode of vibration for experiment and simulation respectively.

$$MAC(r,q) = \frac{\left|\{\varphi_E\}_r^T\{\varphi_S\}_q\right|^2}{\left(\{\varphi_E\}_r^T\{\varphi_E\}_r\right)\left(\{\varphi_S\}_q^T\{\varphi_S\}_q\right)} \tag{3}$$

The MAC is evaluated for the two systems of given parameters in Figure 26. The matrices for each of the folded and planar symmetric zigzag desigs are as follows:

$$MAC_{Folded\ Zigzag} = \begin{bmatrix} 0.954 & 0.025 & 0.002 \\ 0.005 & 0.989 & 0.012 \\ 0.000 & 0.000 & 0.921 \end{bmatrix}$$

and,

$$MAC_{Planar\ Zigzag} = \begin{bmatrix} 0.970 & 0.004 & 0.007 \\ 0.031 & 0.796 & 0.028 \\ 0.047 & 0.009 & 0.988 \end{bmatrix}$$

The values for the diagonal elements of the MAC matrices are indications of strong correlation between the experimetal and simulation results. For the planar symmetric zigzag, the second mode shows lower coherence due to it being a torsional mode, and therefore, not being the most visible in the direction of sensing shown in Figure 21 for the test setup.

6.5 Summary

The FRF plots and modeshapes shown in Figure 29 and Figure 30, along with the MAC values calculated indicate a very good agreement between the test and simulation results as a means of validation for the COMSOL results.

Chapter 7

Strain Node and Frequency Analysis

This chapter explains the dynamic advantages of the proposed design compared to the planar symmetric zigzag design. The ability of the folded design to avoid strain nodes for a smaller aspect ratio is discussed along with the reasoning behind it. Various studies are presented to show the versatility of the design for use in different applications.

7.1 Case Studies and Approaches

This section discusses the effects of various factors such as the unit length, number of legs, number of stories in the folded design, the scale of the design, and the distance between consecutive stories on the strain node pattern.

7.2 Leg Length Variation

The first study involves evaluating the dependence of strain nodes on the length of each leg given that the width of both the designs stays the same. For consistency, no added tip mass is used for the planar symmetric or folded zigzag design. The schematic for the folded zigzag unit is shown in Figure 36, and the dimensions for both the units are listed in Table 4.
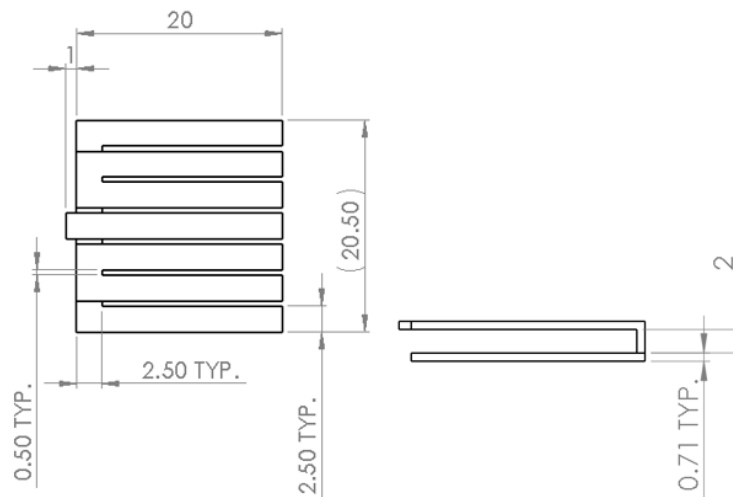
Figure 36 Top and Side view of a Folded Zigzag design used for COMSOL simulations showing all the dimensions in mm

Table 4 Dimensions for folded zigzag and planar symmetric zigzag used for COMSOL analysis

Property	Folded Zigzag	Symmetric Zigzag
Leg length (mm)	20	20
Leg width (mm)	2.5	2.5
Leg thickness (mm)	0.71	0.71
Distance between consecutive legs (mm)	0.5	0.5
Distance between the top and bottom stories (mm)	2	N.A
Total number of Legs	7+5	7

Figure 37 shows how the strain plots and the strain node location change as the length of the two units varies, while keeping all other parameters the same. As the length decreases, as shown in Figure 37, the natural frequency for both the designs increases. The decrease in leg length makes the designs more susceptible to torsion since the width of the designs stays the same. Eventually the torsional mode becomes more dominant and results in strain nodes for both the designs, but at different leg lengths.
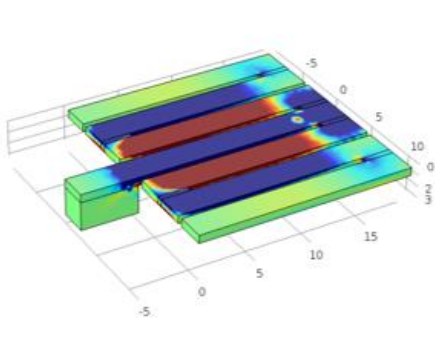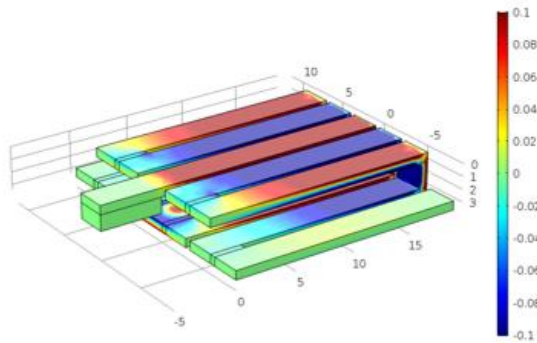
493.1 Hz   258.35 Hz

534.58 Hz   280.09 Hz

35
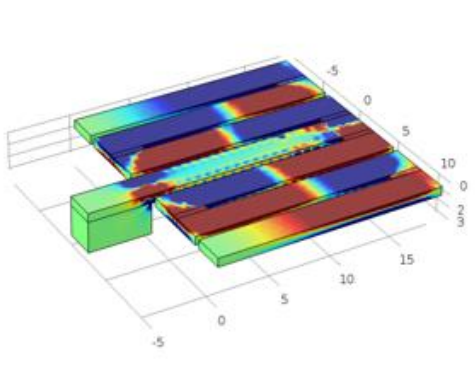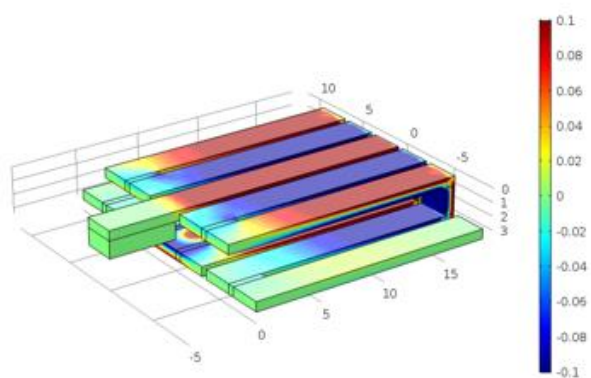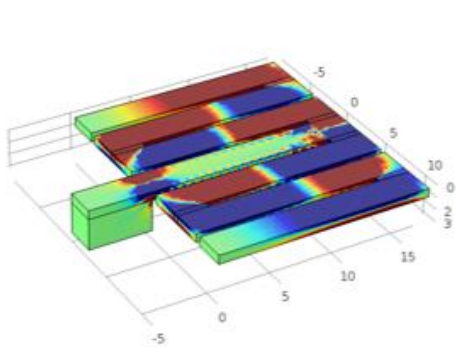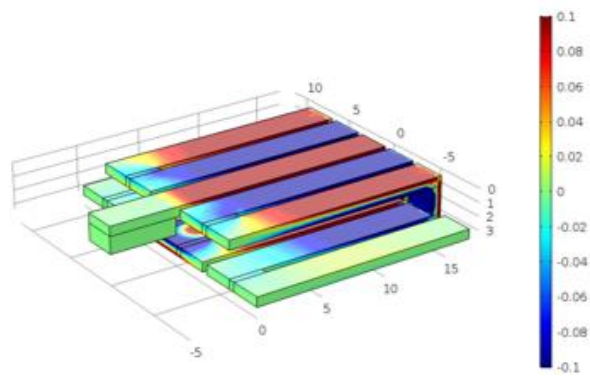
586.03 Hz   317.65 Hz
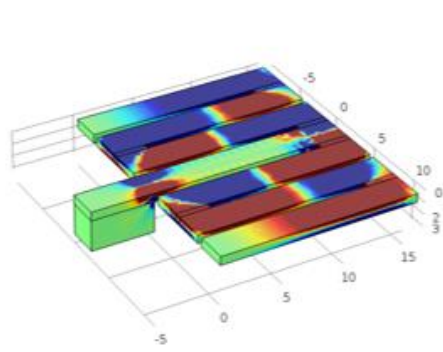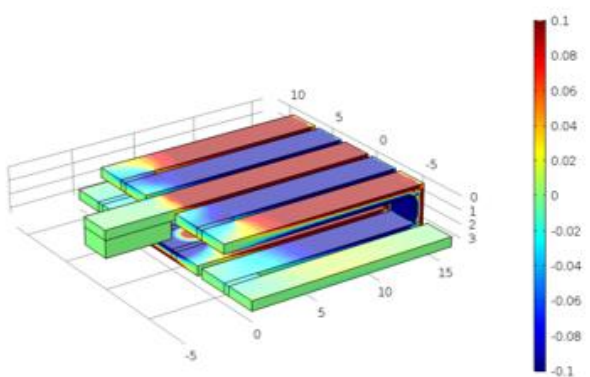
628.73 Hz   355.18 Hz
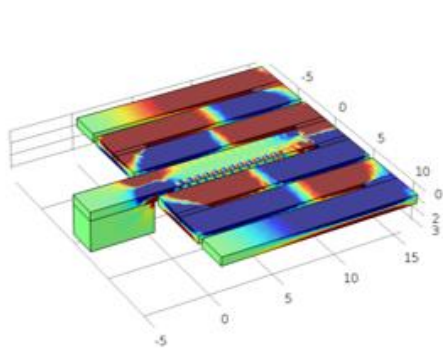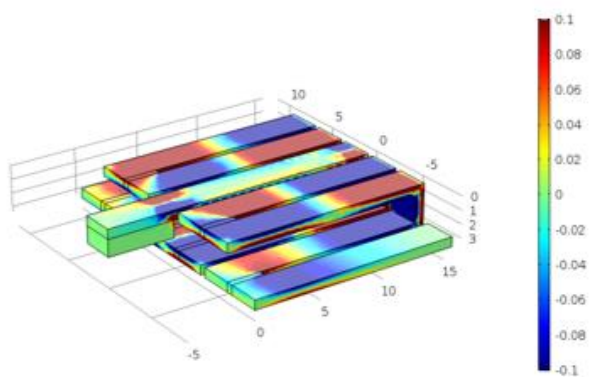
644.63 Hz   366.66 Hz

Figure 37 Strain plots with fundamental frequencies of planar symmetric and folded zigzag for various leg lengths (parallel to the central beam) while keeping the width the same for all the designs. (Top to bottom lengths: 19mm, 18.2 mm, 17mm, 16mm, and 15.7mm)

The strain nodes becomes apparent at a length of about 18.2 mm for the planar symmetric design, whereas this happens at about 15.7 mm for the folded design. The results are performed for smaller length increments but only the lengths of significant importance (i.e. transition from bending to torsion) are shown. The results indicate that the additional story in the design allows for a significantly smaller natural frequency, almost half of the planar design, as well as a smaller minimum length at which the strain nodes are avoided. In order to understand the relation of the unit length to the appearance of the strain nodes, and the dominance of the torsion as a fundamental mode, the frequencies for the first bending and the first torsional modes are found for various lengths for each of the two designs.

Figure 38 shows a plot of the natural frequencies for the first bending and torsional modes for each of the two designs shown in Figure 12-(b) and (c) as the unit length changes. The presented results show that, for a given footprint, the folded zigzag achieves a significantly smaller fundamental frequency of the bending mode when compared to the planar symmetric unit. Additionally, in both units the torsional mode eventually becomes the first mode of vibration as the length decreases below a certain value, resulting in the formation of strain nodes. This is expected as a smaller length results in a unit more susceptible to twist than bending in both designs. The presence of the torsional mode as a fundamental mode will result in the appearance of the strain nodes, which should be avoided for a prudent design. As shown in this plot, the torsional mode is avoided at smaller lengths for folded zigzag design compared to the planar symmetric unit.

Figure 38 Natural frequencies for the first bending and torsional modes for planar symmetric and folded zigzag designs with 7 legs

7.3 Number of Legs

The second study involves evaluating the impact of the number of legs in each design on the footprint size and aspect ratio in order to avoid strain nodes in the fundamental mode. The leg length analysis from the previous section is performed for a 5-leg and 9-leg unit design in this section to study the effects of the number of legs on the strain nodes as the leg length changes. Overall, it is expected that an increase in the number of members will result in a more flexible unit and a smaller fundamental natural frequency for each design. However, with the increased number of legs, the system becomes more susceptible to twist, making the torsional mode more dominant for the fundamental frequency, which consequently results in the appearance of the strain nodes. The number of legs represents the maximum number that one layer can have in a folded zigzag design, not the total number of legs. For example, a 5 leg design means that the top layer has 3 legs and the bottom layer has 5 legs. The results for the different number of legs analysis are summarized in Table 5. As expected from the previous part of the analysis, as the unit length decreases, the torsional mode eventually becomes dominant, which is the start of the appearance of the strain nodes. It is also shown that for units with fewer members, the critical length at which the torsional mode becomes the first mode is smaller. This is expected as a unit of fewer members has a smaller width, and hence is less susceptible to torsion, which

allows for a smaller length for the unit to avoid torsion. Additionally, Figure 39 and 40 show that, as the number of legs decrease, both the designs are getting closer to a simple cantilever configuration for which the bending mode becomes dominant. Also, as described by Karami *et al.* [18], similar behaviour is noted for the zigzag design where the torsional mode appears before the bending mode when the number of legs increases.

Table 5 Critical lengths for units of several legs

Number of legs in a design	Critical length for planar symmetric zigzag (mm)	Critical length for folded 2-story zigzag (mm)
5	12.1	9.9
7	18.2	15.7
9	25.2	21.8
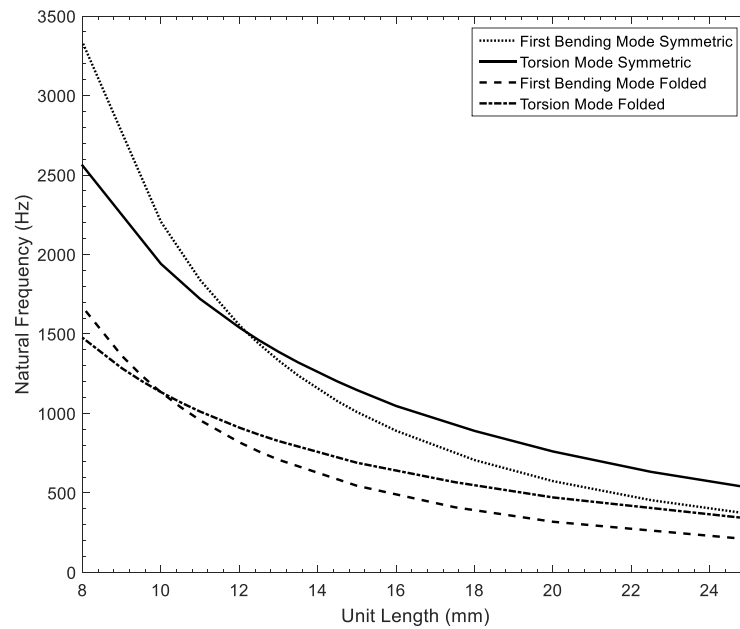
Figure 39 Natural frequencies for the first bending and torsional modes for planar symmetric and folded zigzag designs with 5 legs

39
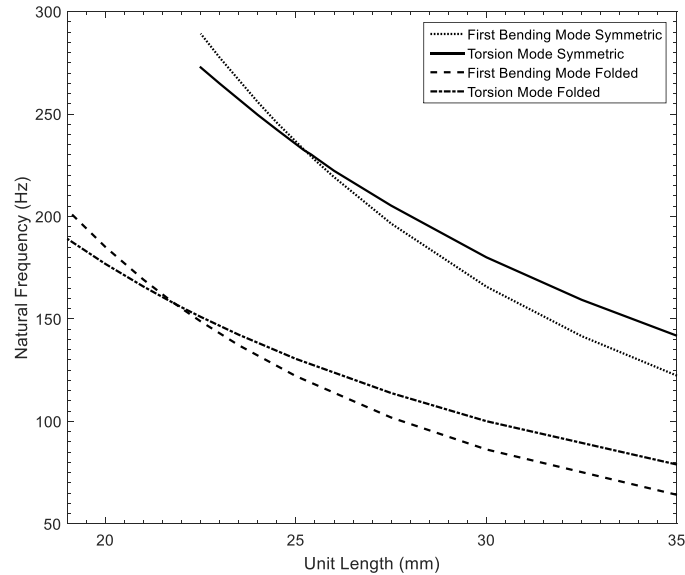
Figure 40 Natural frequencies for the first bending and torsional modes for planar symmetric and folded zigzag designs with 9 legs.

7.4 Design Scale

Another important factor to study in this design relates the impact of the scaling factor on the torsional and bending mode's behaviour for each unit. Figure 41 presents such results for both units when the geometric values shown in Table 4 are scaled down by factor of 10. As shown in Figure 41, a similar trend is noted for both designs. The natural frequency is increased by a factor of 10 as expected from a much smaller unit. Interestingly, the critical length at which the torsional mode becomes the dominant mode of vibrations for each of the two units is also scaled down by the same factor.

On the other hand, when the footprint of both the designs is scaled up, the behaviour of the vibrational modes changes for the folded zigzag design. As the footprint scales up, the design becomes torsionally dominant for the fundamental mode of vibration. By contrast, the planar symmetric zigzag configuration shows the same behaviour while scaling up as it did when it scaled down. The plot below, Figure 42, shows the natural frequency behaviour for the folded zigzag and the symmetric zigzag design when they are scaled up by factor of five from the parameters in Table 4. Once again, the ratio at which the torsional mode becomes dominant stays the same as the original scale for both the designs.
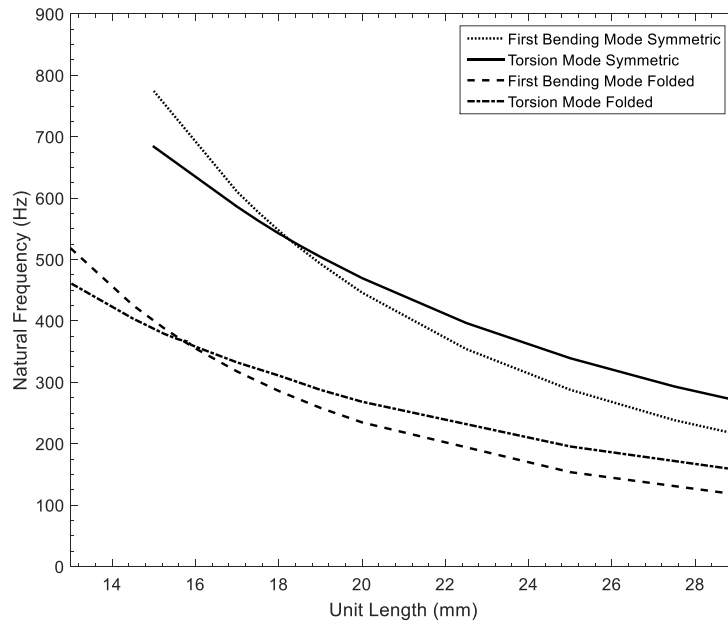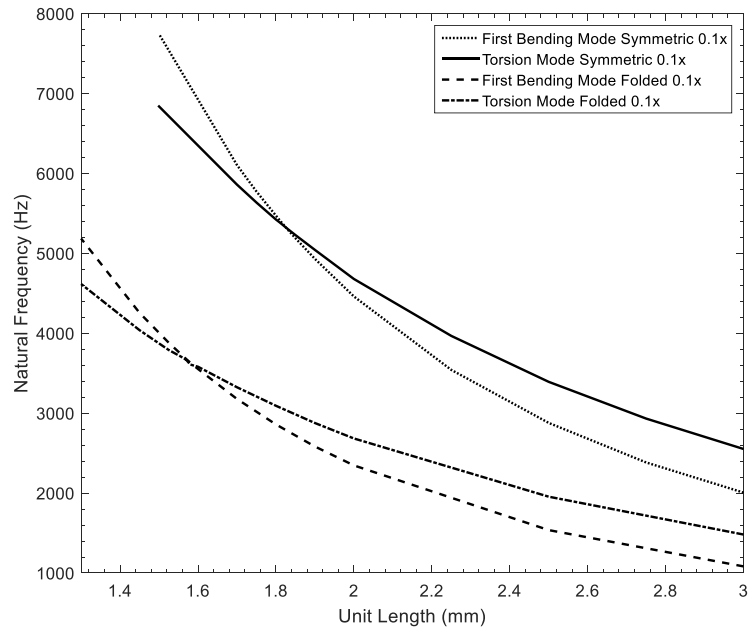
Figure 41 Natural frequencies for the first bending and torsional modes for planar symmetric and folded zigzag 7 leg designs scaled down by a factor of 10
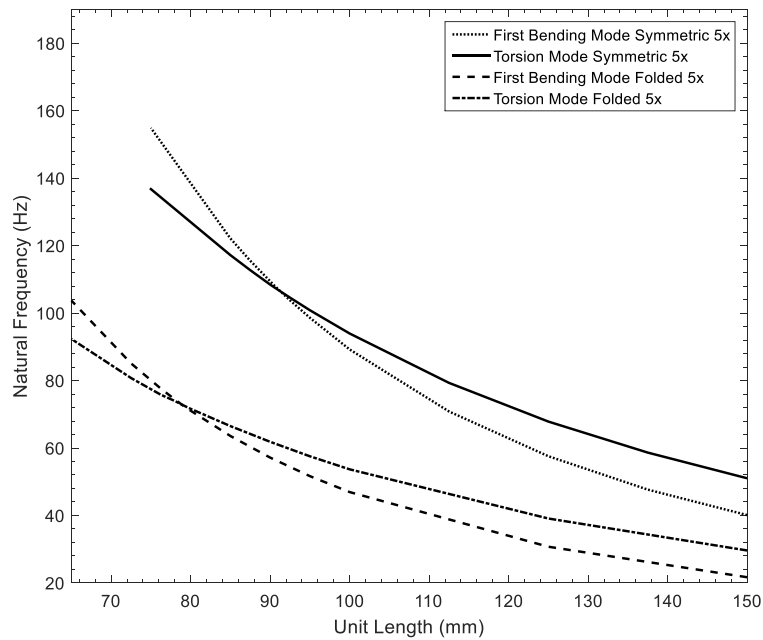
Figure 42 5x scaled up planar symmetric zigzag and folded zigzag 7-leg frequency analysis

7.5 Number of Layers

The results shown in the previous analysis clearly demonstrate the advantages of the folded zigzag design for both the strain nodes pattern, and the significant reduction of the unit's fundamental natural frequency for a given footprint. This analysis studies the impacts of number of stories and the distance between them on the system's dynamics. For this purpose, 7-leg folded zigzag designs with 2, 3, 4 and 5 stories are studied. With the increase in number of stories, the total number of legs also increases but the maximum number of legs remains the same, which is seven. Hence, for a 4-storied design, the number of legs is the maximum in the bottommost layer, being 7, and 5 for the other three layers.

Figure 43 shows the fundamental bending natural frequencies for each of these units at various lengths. With all the other geometric factors remaining the same as listed in Table 4, Figure 44 shows a clear advantage in having a unit with a larger number of stories. It is shown that adding these additional stories results in a significantly more flexible unit with a much smaller natural frequency for a given length.
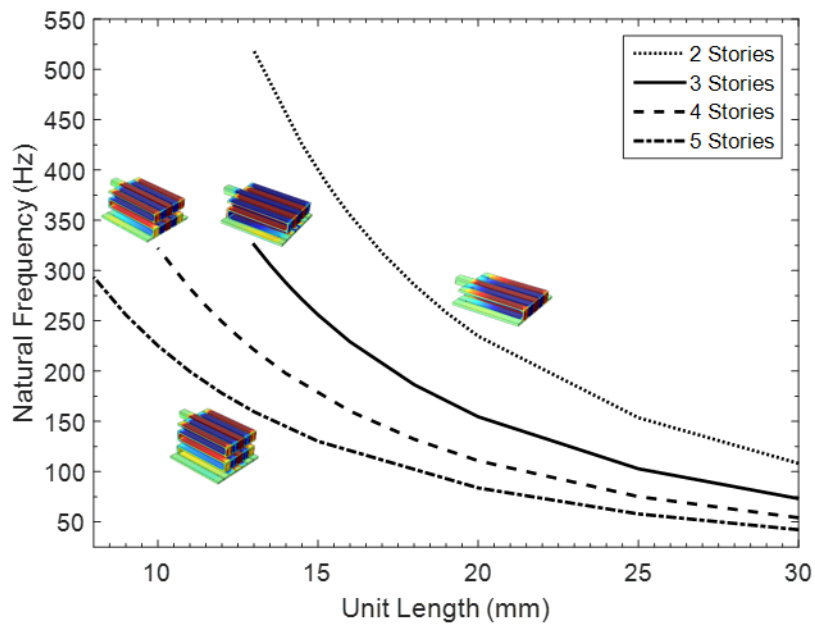
Figure 43 Fundamental frequency of folded zigzag with respect to the number of stories

Another important aspect to consider is how the critical length for which the torsional mode becomes the first mode changes as the number of stories is increased. The critical length values are shown in Figure 44 indicating the advantage of the additional stories used.
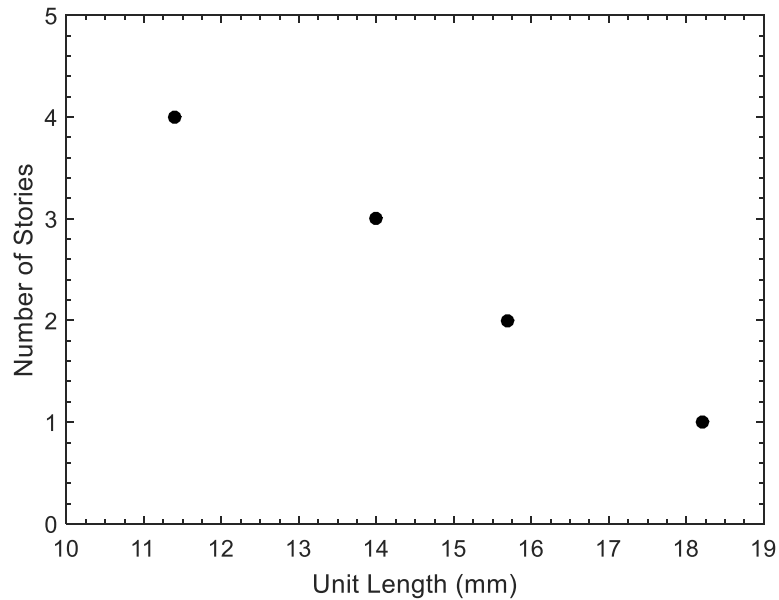
Figure 44 Critical lengths for 7-leg folded zigzag units of different stories

During the previous study, interesting behaviour was observed for the 5-story design and is presented in Figure 45. Previously, the critical lengths were found using the length for the intersection point between the bending and torsional modes. This is the point at which the torsional frequency will become smaller than the bending. In the results for the 5-story unit shown below, the torsional frequencies become tangent to the bending, but never become smaller. This indicates that for this unit the torsional mode never becomes dominant as the unit length gets smaller, so bending will remain the first mode of vibrations, making this an ideal design for avoiding the strain nodes. It is expected that for larger number of stories the first torsional mode plot will become detached from the first bending plot and remain at higher values than the bending frequencies for all lengths.
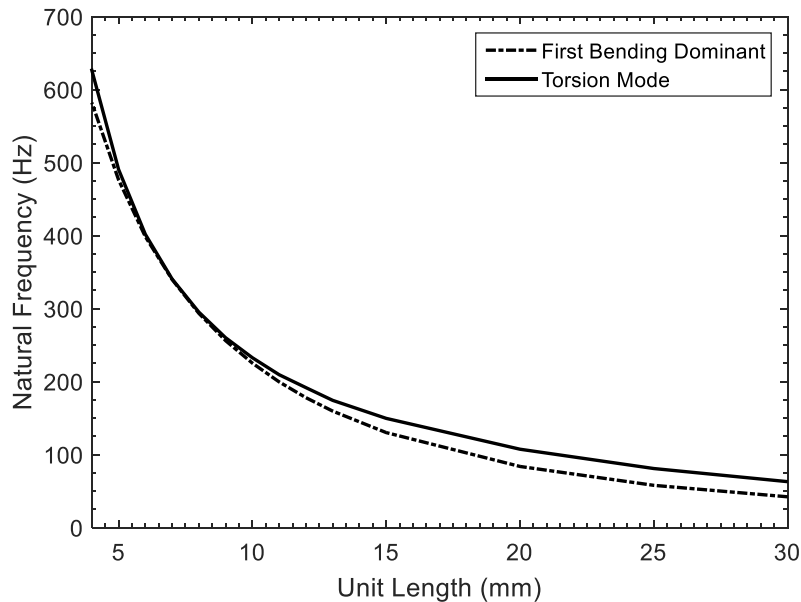
Figure 45 Natural frequencies for the first bending and torsional modes for a 7-leg, 5-story design

7.6 Distance between Layers

Another interesting aspect to consider in the design is how the distance between the stories can affect the dynamics of the system. This section describes the analysis performed on a 2-story folded zigzag design with variable spacing between the two layers. In this study, the spacing is varied from 2mm to 8mm at 2mm increments. As evident from Figure 46, increasing the distance between the stories results in a smaller natural frequency due to an overall larger effective length and a more flexible unit.

This frequency reduction is shown to be at a much smaller rate than having an additional story in the gap between the top and bottom layers. However, this design can be used in cases where collision between the layers may be a concern during the vibrations. It is also noted that with the increase in the length of members, the natural frequency starts converging, as the behaviour becomes independent from the number of stories and the distance between the stories. For much larger lengths, the effect of stories on the natural frequencies is not prominent as the configuration becomes more cantilevered rather than folded.

44
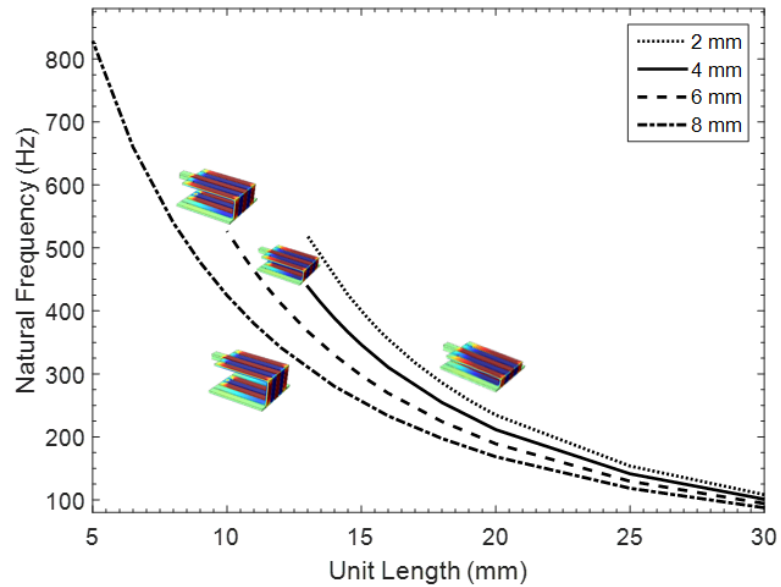
Figure 46 Bending natural frequency for 2-story folded zigzag units of different layer spacing

Similar to the multi story analysis, the critical length of variable spacing, shown in Figure 47, between two stories is also plotted to show when the torsional mode becomes the fundamental mode.
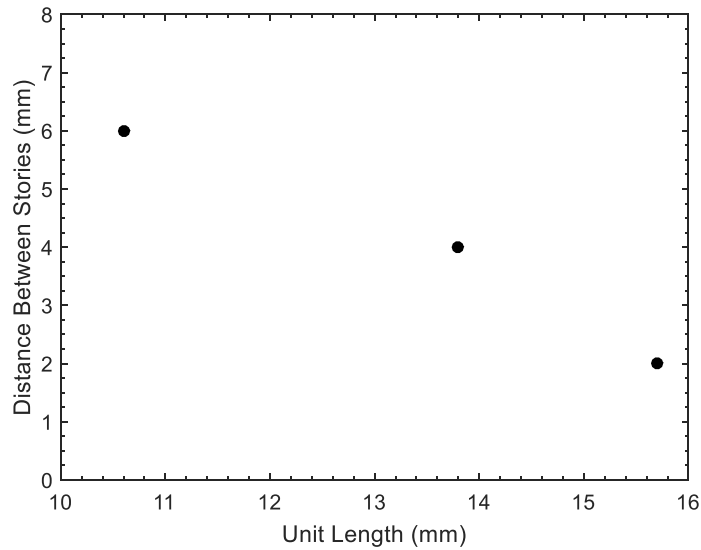
Figure 47 Critical lengths for 7-leg folded zigzag units of variable distance between two stories

Once again, interesting behaviour is noted for the design with 8 mm spacing between the two stories. In the results for 8mm spacing shown in Figure 48, the torsional frequencies become tangent to the bending, but never get smaller. This indicates that, for this unit, bending remains the fundamental mode

of vibration irrespective of the length of each member, making it an ideal design for energy harvesting while avoiding strain nodes.
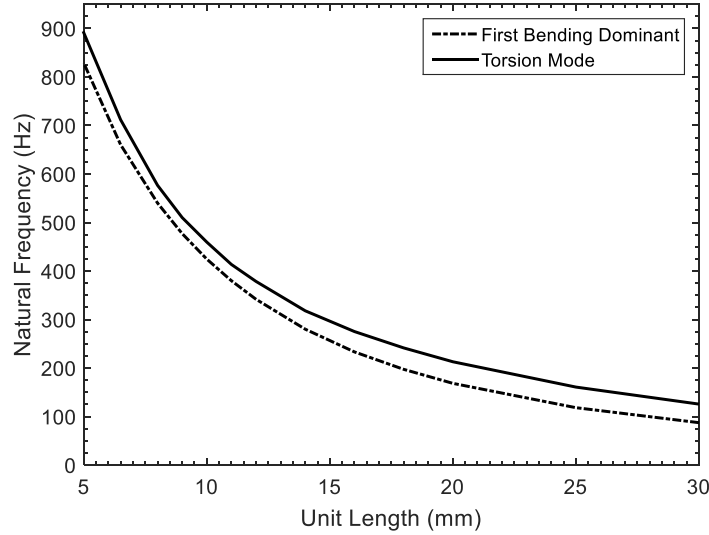
Figure 48 Natural frequencies for the first bending and torsional modes for a 7-leg, 2 story with 8mm spacing design

7.7 Summary

The suggested design offers an attractive option for a 3-dimensional geometry in which the addition of the third dimension takes the form of an added story. This additional story helps with both achieving a smaller fundamental natural frequency and an improved strain node pattern at smaller footprints. For a 2-story design, the strain nodes are removed when the unit's length is the same as its width. The strain nodes begin to appear when the length further reduces below the width and the aspect ratio decreases. As the number of legs increases, both designs show a decrease in their natural frequencies, but an increase in the aspect ratio at which the strain nodes start to appear. This increase is greater for the planar symmetric zigzag than the folded zigzag. It is also shown that additional stories in a folded zigzag can help further reduce the natural frequencies and the minimum critical length for a given footprint to avoid the strain nodes.

46

Chapter 8
Model Validation with PZT

In this chapter, the final numerical model is verified using the experimental results. Initially, the natural frequencies are compared and percent error is evaluated to show the applicability of the numerical simulation. In addition, the displacement, voltage and power FRFs are also compared to show the agreement between the numerical and experimental results. The optimal resistance is also calculated from both the experiments and the simulation, and the results are compared.

8.1 Purpose

The purpose of this chapter is to validate the modelling of a complex 3D energy harvester. The simulation results are compared with the experimental results to draw conclusion about the model. Once the model is validated for a complex geometry, conclusions are drawn from simpler models for comparison purposes without performing experimental tests.

8.2 Experimental and Simulation Displacement Comparison and Damping

In this section, the displacement data from the simulation is compared with the experimental results to show the agreement between the two for the folded design with PZT strips and tip masses. In addition, it briefly describes the evaluation of damping ratios using the peak method. Figure 49 compares the displacement FRF of experimental data and the undamped COMSOL simulation data. It is evident from the figure that natural frequencies predicted by COMSOL are approximately the same as the experimental natural frequencies. Table 6 shows the percent error between the experimental and COMSOL natural frequencies, which demonstrates the promising results predicted by the simulation for the first three modes of vibration having a maximum percent error of 1.04%.
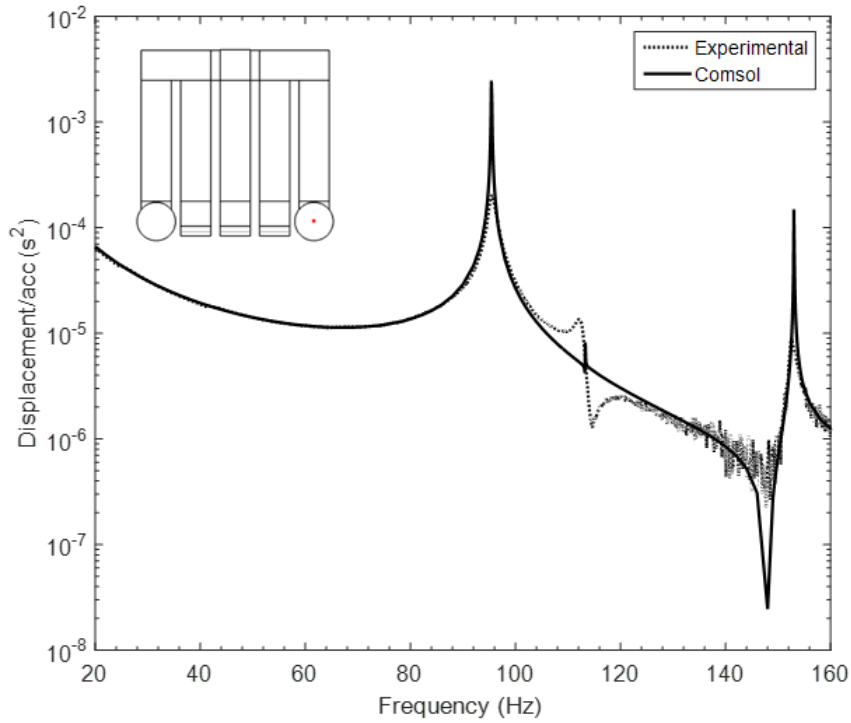
Figure 49 Displacement comparison between experimental and undamped COMSOL results showing torsional mode

Table 6 Experimental vs. COMSOL natural frequency comparison

Natural Frequency (Hz)	Run	COMSOL	Experimental	Percent Error
First Mode	**Top Layer**	95.6	95.6	0.052
	Bottom Layer	95.5	95.6	0.052
Second Mode	**Top Layer**	113.3	113.7	0.352
	Bottom Layer	113.3	113.1	0.177
Third Mode	**Top Layer**	154.0	153.5	0.326
	Bottom Layer	155.0	153.4	1.043

To evaluate damping, the peak method described by Inman is used [37]. The peak method analysis is performed on the two bending natural frequencies, which are the first and the third mode of vibration for this design. Table 7 shows the damping ratios evaluated using experimental results and used in the COMSOL simulations.

Table 7 Evaluated damping ratios using the peak method

Damping Ratio	Percentage
ζ_1	0.628 %
ζ_2	0.407 %

After adding damping to the simulation, the displacement plots for when the top and bottom layer are wired separately are presented to show the coherence between the dynamics of the experiments and the simulation. The tip displacement is plotted for the 10^4 Ω resistance value for both top and bottom layer. Damping ratios evaluated previously are used in the simulation for all the upcoming results. Figure 50 and 51 show the comparison between the experimental FRF and simulation FRF obtained at the center of the right tip magnet when the external resistance is 1E4 ohms. As mentioned before, with the addition of damping to the simulation the second mode of vibration, dominantly torsional, is damped out from the simulation results. It is evident from the figures below that the displacement behaviour is characterized well by the simulation for the first three modes. The presence of noise for the higher modes in the displacement plot is due to low base acceleration. The base acceleration is decreased in the proximity of natural frequencies to acquire a clean voltage response FRF without over straining the PZT layers.
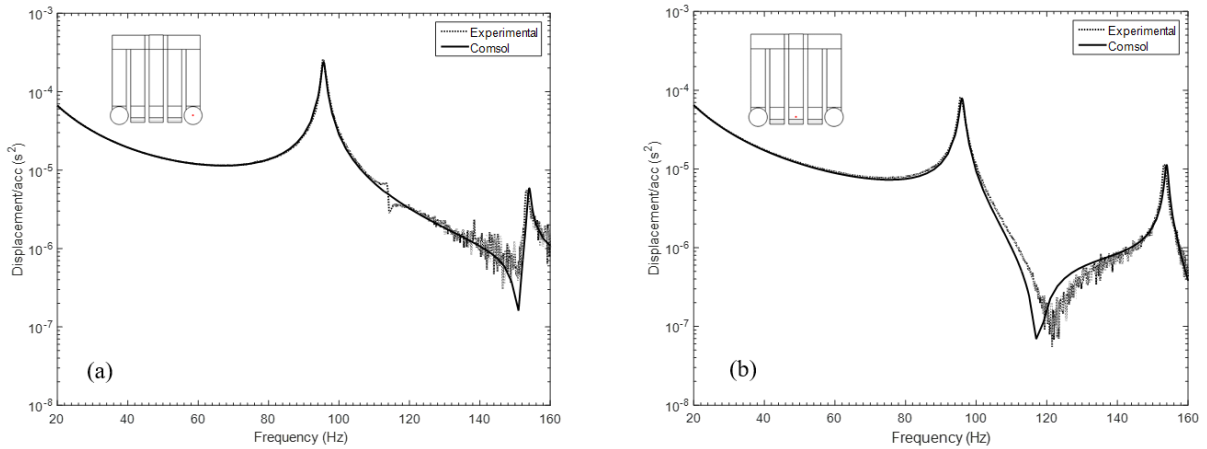
Figure 50 Damped (a) right tip displacement (b) center displacement FRF comparison for Top layer
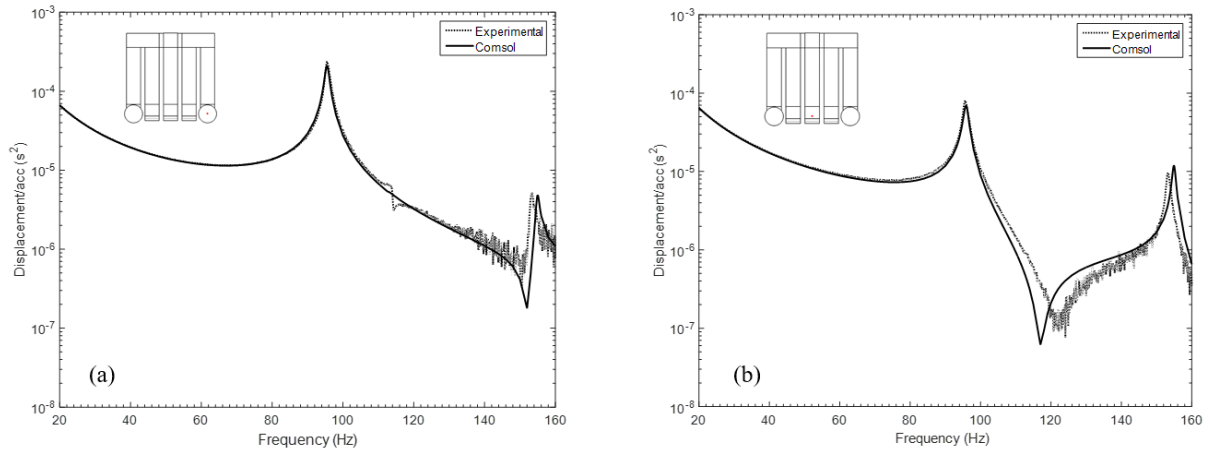
Figure 51 Damped (a) right tip displacement (b) center displacement FRF comparison for Bottom layer

8.3 Experimental and Simulation Voltage Comparison

To gain confidence in the COMSOL simulation, this section compares the voltage output results obtained from the experiments with the simulation results. The previous chapters analyzing this design on strain node generation validated the solid mechanics aspect of the simulation by evaluating Modal Assurance Criterion (MAC) between the experimental and simulation modeshapes. With the addition of an electrostatic module and the electric circuit module in COMSOL to predict the output voltage and power, the simulation becomes more complex. Hence, it is necessary to validate the outcomes from the simulation before any comparisons are made between different designs.

In order to show the applicability of the simulation, multiple resistance values (i.e. external loads) are used and the optimal resistance value is experimentally acquired. The optimal resistance value is obtained by the process of impedance matching. Impedance matching is a condition when the load resistance (external resistive load, in this case the resistor box) is equal to the source resistance (beam or design impedance) [38]. Challa *et al.* exploits the analytical expression of power for a stand-alone piezoelectric energy harvester to define impedance matching [38]. The external resistance used at this condition is referred to as the optimal resistance and the power output is maximum at this resistance. The optimal resistance is evaluated experimentally using the resistor box, shown in Figure 21, by performing the load sweep analysis for both layers. With the difference in the number of legs for the top and the bottom layer, the optimal resistance is expected to be different as well.

The voltage FRF plot for both the top and the bottom layer is shown for four different resistances (10^2 Ω, 10^3 Ω, 10^4 Ω and optimal). The optimal resistance value for the top and bottom layer is

approximately 6.3 x 10^4 Ω and 8.0 x 10^4 Ω respectively found using experimental and COMSOL load sweeps.

Similar to the displacement plots, the voltage obtained from the experimental results is compared against the simulation voltage. This comparison is also performed over the first three modes to illustrate the ability of simulation in predicting the behaviour of voltage response for higher modes. Figure 52 and 53 compare the voltage output at different resistances for both top and bottom layer of the folded zigzag design. As intuitively obvious, with the increase in external resistance, the voltage output increases, and follows the Ohm's law.

The simulation does a tremendous job of predicting the voltage from the piezoelectric strips pasted on this complex three-dimensional geometry. The differences in the experimental and simulation voltage may be related to the manufacturing process used to create the energy harvester. In addition to that, the epoxy applied to adhere the PZT to the substrate is too complex to be modelled in COMSOL and is ignored. The wires used to make the connections in the experiment and the electrical tape alter the mass and stiffness of the structure, creating further discrepancies in the results. Finally yet importantly, using SMP for experiments and SME for simulations might also have altered the results.
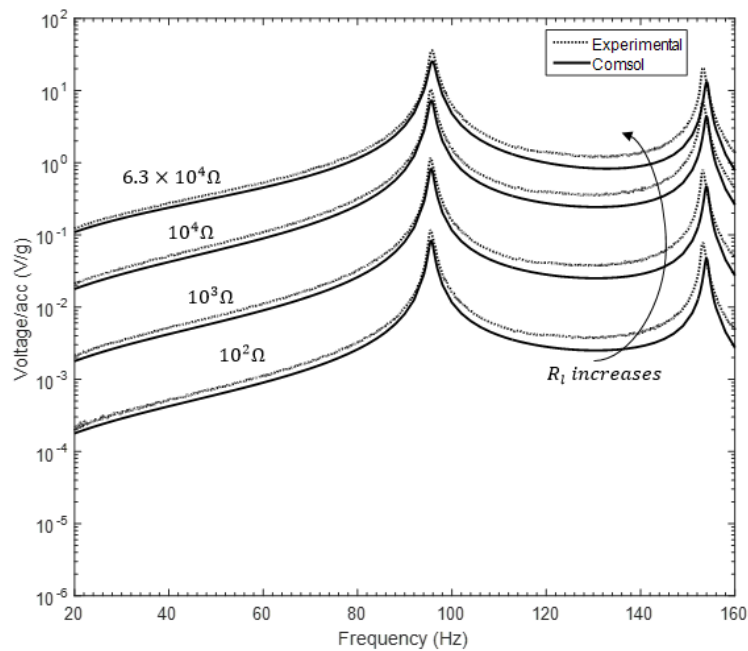
Figure 52 Voltage FRF comparison between experimental and simulation run at different resistances for top layer
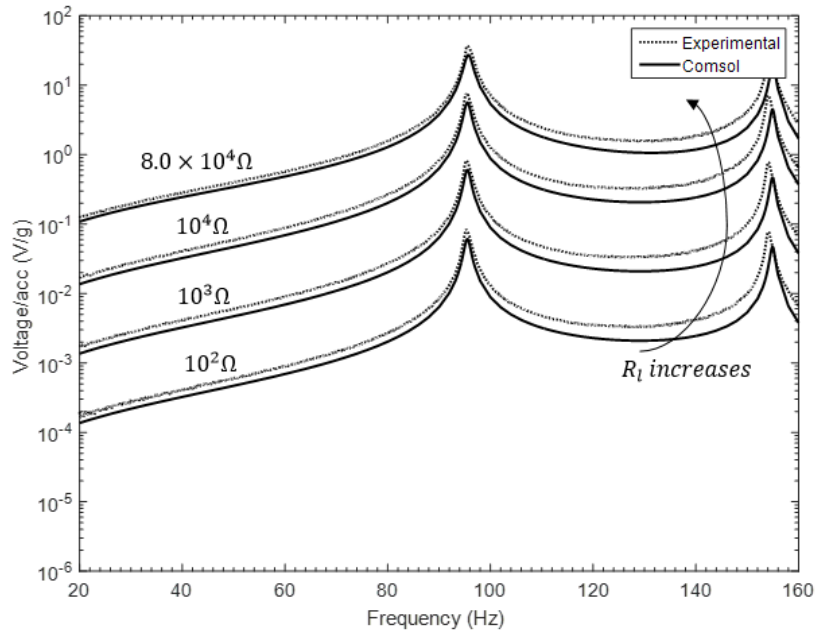
Figure 53 Voltage FRF comparison between experimental and simulation run at different resistances for bottom layer

8.4 Experimental and Simulation Power Comparison

The power output of the experimental and simulation run is compared to show the agreement between the results. The results are shown for a 100 Ω's resistance, optimal resistance and resistance higher than the optimal resistance. The plotted results confirm that the previously stated optimal resistance is in fact the resistance producing the maximum power. The comparison is shown in Figure 54 and 55 for both the top and the bottom layer respectively.

It is evident that the power output is maximum for the optimal resistance and decreases for resistance values higher or lower than this. The reason behind a larger error between the experimental and simulation results is because the voltage results are squared to get power ($P = V^2/R$) resulting in a larger magnitude difference between the two results.
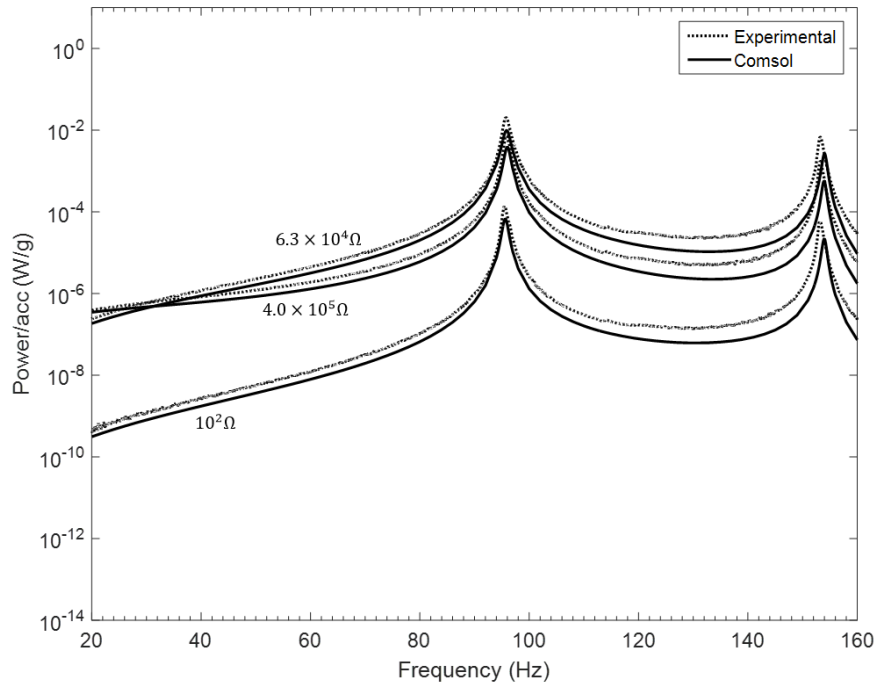
Figure 54 Power output comparison for Top layer of Folded Zigzag at different resistances
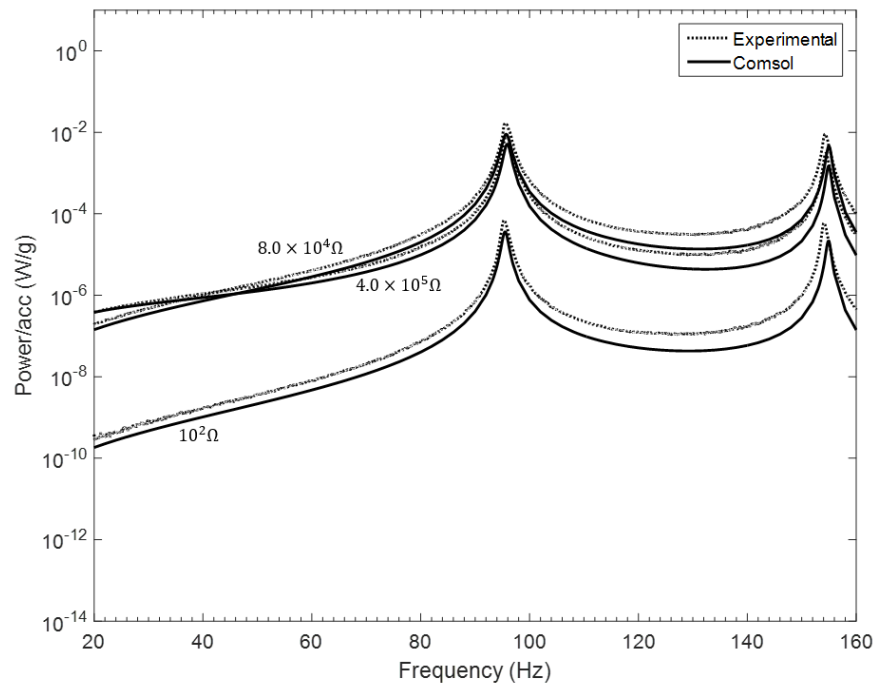
Figure 55 Power output comparison for Bottom layer of Folded Zigzag at two different resistances

8.5 Summary

The previously presented comparisons between the displacement, voltage and power FRFs demonstrate that the simulation successfully predicts the mechanical and electrical behaviour of a complex folded structure. Therefore, the results from the simulation for simpler geometries, such as flat symmetric zigzag, can be trusted without performing experimental analysis. This allows the power output from the new design and the already existing planar symmetric zigzag design to be compared with confidence [39].

Chapter 9

Power Comparison

In this chapter, the COMSOL simulations are used to compare previous designs with the proposed design. Four different cases are used for the planar symmetric zigzag for different types of comparisons. Finally, the advantage of using a tip mass to increase the power output is also discussed.

9.1 Case Studies and Approaches

The final section of this thesis compares the power of the new folded zigzag design and the planar symmetric zigzag, strictly based on the results from the COMSOL simulations after verifying their applicability in the previous section. To allow a fair and meaningful comparison, the power comparison is to be performed at each design's optimal resistance and damping is removed from all the models. Table 1 shows the substrate geometry, PZT geometry, and PZT type for the folded design, which is kept the same for the COMSOL simulation of the planar symmetric zigzag design. As shown in the previous chapters, the fundamental natural frequency for the planar symmetric design is higher than the folded design. Hence, to compare the power output of the two units, overlaying the power FRF's on each other is simply not enough. Therefore, four different design scenarios are used to compare the power output of the two designs.

9.2 First Case

In order to make a fair and conservative comparison, the folded zigzag design is compared against two planar symmetric zigzag designs in the first case. The two planar symmetric designs represent each layer of the folded design. In this case, the footprint and the total tip mass are kept the same for both designs, which results in different natural frequencies. Each planar symmetric unit has half of the tip mass compared to the folded design to keep the total tip mass the same. The power output in this case is compared by taking a bandwidth around the peak and evaluating the area underneath the peak divided by the bandwidth.

$$Power\ (W) = \frac{Area\ under\ the\ peak\ (W.Hz)}{Bandwidth\ (Hz)} \tag{4}$$

$$Power\ Density\ \left(\frac{W}{m^2}\right) = \frac{Power}{Harvester\ Area} \tag{5}$$

This analysis is performed for both the top and the bottom layer as shown in Figure 56 and the results are compared with the planar symmetric design power output shown in Figure 57. This is a conservative comparison of power from the folded and two planar symmetric zigzag designs to show that two planar symmetric zigzags stacked on top of each other with the same total tip mass will have a lower total power density than a single folded zigzag design.
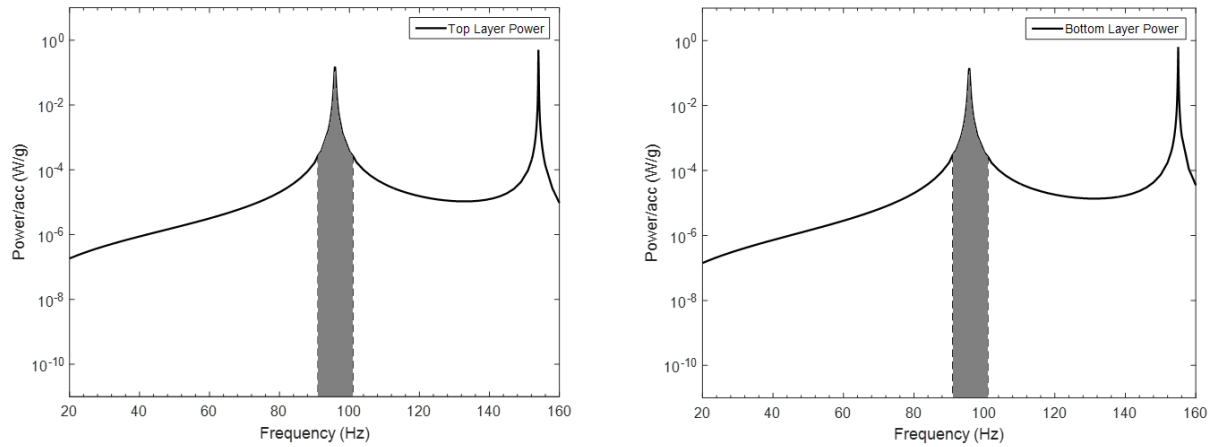
Figure 56 Folded Zigzag area under the fundamental natural frequency for 10 Hz bandwidth of power output for Top (left) and Bottom (right) layer
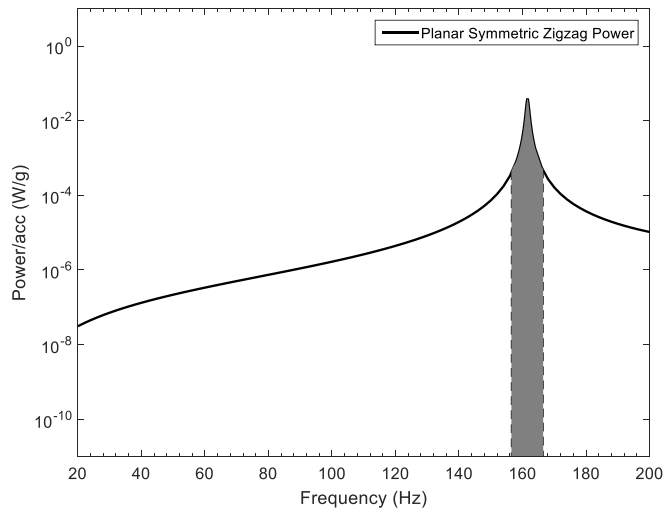
Figure 57 Planar Symmetric Zigzag area under the fundamental natural frequency for 10 Hz bandwidth of power output

In addition, as evident from Table 8, only three legs of the bottom layer of the folded design produce more power in the proximity of a resonance peak compared to a 5 legged planar symmetric zigzag design. The results depict that both the top and bottom layer are individually producing more power around the fundamental natural frequency, making the folded design an attractive option.

9.3 Second Case

The second comparison investigates the power density from a planar symmetric zigzag design when the tip mass is the same as for the folded zigzag design while the natural frequencies are still different. This comparison also compares one folded unit against two planar symmetric units. The tip mass in this case is the same for all the three units, one folded and two planar symmetric. Hence, the total tip mass for the two planar symmetric units being compared is double the tip mass used for the folded design as shown in Table 8. The results in It should be noted that the power output from two units of the third comparison (Planar Symmetric Zigzag, heavy tip mass) is higher than the proposed design due to the advantage produced by larger tip mass per unit layer. In this regard, it is worthy to note that even a clamped-free beam with a tip mass can offer a higher power than any of these units if the beam's length or the tip mass are sufficiently increased. However, this defies the incentive of seeking a more flexible design while being compact, which has commonly been sought for energy harvesting applications to avoid the need for a large tip mass or a large footprint for tuning the natural frequency. Also, it should be noted that adding more layers to the proposed design will eventually remove the need for adding the tip mass for the frequency tuning, which is another attractive feature of the proposed design. Finally, it should be recognized that if only one unit of any of the designs shown in this paper is compared to one unit of the folded zigzag for power output comparisons, the proposed folded zigzag would still have an advantage.

Table 8 also show that even with the same tip mass, the folded design is still able to produce a higher power density.

9.4 Third Case

Another variation of tip mass is analyzed in the third comparison where the tip mass for a single planar symmetric unit is increased until its natural frequency matches that of the folded design. Table 8 shows that the tip mass required for the planar symmetric design to achieve the same natural frequency as the folded design is almost double, indicating the increased flexibility of the proposed design. The reason for comparing the folded design against only one planar symmetric design in this case is discussed later in this chapter.

9.5 Fourth Case

The final case compares the folded zigzag design with two of the planar symmetric designs while keeping the same natural frequency and total tip mass. As seen in the first comparison, using constant total tip mass results in different natural frequencies for the designs. Therefore, the geometry is modified to achieve the same natural frequency. This is done by extending the middle leg of the planar symmetric design to increase flexibility until the frequency of the harvester matches the natural frequency of a folded zigzag design. The PZT on the middle leg is also extended, shown in Figure 58, so the distance between the clamp and the front end of PZT on the middle leg is same for both units. The middle leg is extended instead of the legs with the tip mass to be conservative as the strain is maximum in the middle leg, and extending the PZT over this entire additional area gives this design another advantage.
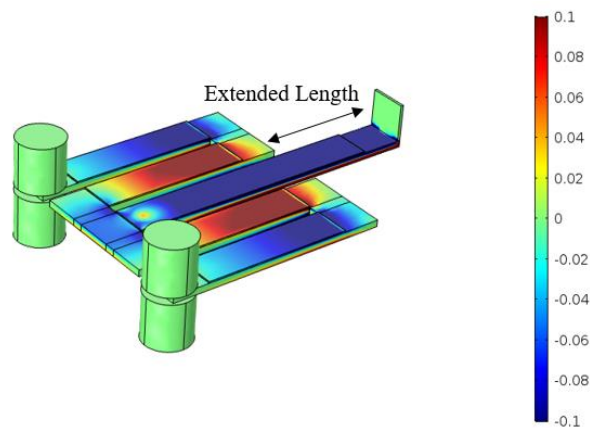
Figure 58 Planar Symmetric Zigzag showing extended length for power output comparison

The power density of the two designs is compared in a similar manner by calculating the area under the resonance peak for 10 Hz bandwidth. As shown in Table 8, two units of planar symmetric zigzag with extended leg having the same natural frequency and same total tip mass, produce less power density than a single folded zigzag unit.

9.6 Overall Comparison

It should be noted that the power output from two units of the third comparison (Planar Symmetric Zigzag, heavy tip mass) is higher than the proposed design due to the advantage produced by larger tip mass per unit layer. In this regard, it is worthy to note that even a clamped-free beam with a tip mass can offer a higher power than any of these units if the beam's length or the tip mass are sufficiently increased. However, this defies the incentive of seeking a more flexible design while being compact, which has commonly been sought for energy harvesting applications to avoid the need for a large tip mass or a large footprint for tuning the natural frequency. Also, it should be noted that adding more layers to the proposed design will eventually remove the need for adding the tip mass for the frequency tuning, which is another attractive feature of the proposed design. Finally, it should be recognized that if only one unit of any of the designs shown in this paper is compared to one unit of the folded zigzag for power output comparisons, the proposed folded zigzag would still have an advantage.

Table 8 Power Density comparison at 1g acceleration between folded zigzag and different versions of planar symmetric zigzag design

Design	Number of units	Total tip mass (g)	Power/unit (W)	Total Power (W)	Total Power Density (W/m^2)	Percentage change
Folded Top Layer	1	5.86	9.56E-03	1.88E-02	20.2	-
Folded Bottom Layer			9.20E-03			
Planar Symmetric Zigzag	2	5.86	5.80E-03	1.16E-02	12.46	62%
Planar Symmetric Zigzag same tip mass	2	11.72	9.05E-03	1.81E-02	19.45	4%
Planar Symmetric Zigzag heavy tip mass	1	10.98	1.46E-02	1.46E-02	15.68	29%
Planar Symmetric Zigzag extended leg	2	5.86	9.58E-03	1.92E-02	14.44	40%

Chapter 10

Conclusion and Future Steps

10.1 Conclusion

With the growing need to decrease the size of an energy harvester while keeping a low natural frequency and high power density, different geometries of energy harvesters have been proposed. This paper analyzed a folded zigzag geometry, which is derived from the planar symmetric zigzag design. Compared to the old 2-D design, the folded zigzag takes advantage of the third dimension. By folding the zigzag on top of itself, the flexibility of the design can be altered, resulting in a design with a lower natural frequency than the conventional zigzag for the same footprint, hence making it more suitable for energy harvesting applications. With the increased flexibility, the design also achieves a higher power density when compared to a planar symmetric zigzag. When the power density for a given bandwidth around the first resonance peak is compared, both the top and bottom layers have a higher power density than a planar symmetric zigzag design. The top and the bottom layer produce $10.3 \frac{W}{m^2}$ and $9.89 \frac{W}{m^2}$ of power density for a bandwidth of 10 Hz around the resonance peak for 1g acceleration. With the increased power output for a given area and a lower natural frequency, the folded zigzag design shows potential to be the future for wireless sensor nodes (WSNs).

10.2 Future Steps

In addition to using this design for harvesting energy from ambient vibrations, the frequency can be tuned using a tip mass or modifying the number of layers to harvest energy from power lines. This can be achieved by using a bar magnet as a tip mass and clamping the design over a wire carrying AC current. The magnetic field of the magnet will interact with the changing magnetic field of the current carrying wire, producing a force on the magnet in the z-axis. This force causes the harvester to vibrate and produce energy.

The electrical aspect of this design can be improved by creating complex simulations in COMSOL that can combine the wiring for both the layers. This analysis can then be extended to designs with multiple layers and combining all the PZT strips into one circuit without having any voltage cancellation.

Moreover, design iterations can be performed to investigate the effect of adding additional stories and the distance between stories on the power output from the design. Optimization analysis can then be performed to produce maximum power based on the application of the design.

61

References

[1]   Akyildiz, I. F., Su, W., Sankarasubramaniam, Y., and Cayirci, E., "Wireless sensor networks : a survey," *Computer Networks*, vol. 38, pp. 393–422, 2002.

[2]   Noel, A. B. *et al.*, "Structural Health Monitoring Using Wireless Sensor Networks - A Comprehensive Survey," *IEEE COMMUNICATIONS SURVEYS & TUTORIALS*, vol. 19, no. 3, pp. 1403–1423, 2017.

[3]   Leland, E. S., Lai, E. M., and Wright, P. K., "A Self-Powered Wireless Sensor for Indoor Environmental Monitoring," pp. 1–5.

[4]   Paprotny, I., White, R. M., Wright, P. K., Sciences, C., and Sensor, B., "Modeling, Design and Fabrication of MEMS AC Energy Scavenger for Smart Grid Applications," in *Prceeding for PowerMEMS*, 2010.

[5]   Sodano, H. A., Inman, D. J., and Park, G., "Comparison of Piezoelectric Energy Harvesting Devices for Recharging Batteries," *Journal of Intelligent Material Systems and Structures*, vol. 16, no. 10, pp. 799–807, 2005.

[6]   Kim, H., Lee, W., Dias, H. V. R., and Priya, S., "Piezoelectric Microgenerators — Current Status and Challenges," *IEEE Transactions on Ultrasonics, Ferroelectrics, and Frequency Control*, vol. 56, no. 8, 2009.

[7]   Reilly, E. K., Miller, L. M., Fain, R., and Wright, P., "A Study of Ambient Vibrations for Piezoelectric Energy Conversion," in *Proceedings for PowerMEMS2009*, pp. 312–315.

[8]   Cook-Chennault, K. A., Thambi, N., and Sastry, A. M., "Powering MEMS Portable Devices — A Review of Non-Regenerative and Regenerative Power Supply Systems with Special Emphasis on Piezoelectric Energy Harvesting Systems," *Smart Materials and Structures*, vol. 17, 2008.

[9]   ADT, E., Miller, L. M., E, H., Wright, P. K., and Mitcheson, P. D., "Which is better , Electrostatic or Piezoelectric Energy Harvesting Systems ?," in *Proceedings of PowerMEMS2015: Journal of Physics: Conference Series (JPCS) vol. 660, 012128*, 2015.

[10]   Leland, E. S., Wright, P. K., and White, R. M., "A MEMS AC Current Sensor for Residential and Commercial Electricity End-Use Monitoring," *Journal of Micromechanics and Microengineering*, vol. 19, no. 9, pp. 241–244, 2009.

[11]   Erturk, A. and Inman, D. J., "An Experimentally Validated Bimorph Cantilever Model for Piezoelectric Energy Harvesting from Base Excitations," *Smart Materials and Structures*, vol.

18, no. 25009, pp. 1–18, 2009.

[12]   Roundy, S. and Wright, P. K., "A Piezoelectric Vibration Based Generator," *Smart Materials and Structures*, vol. 13, pp. 1131–1142, 2006.

[13]   Dhakar, L., Liu, H., Tay, F. E. H., and Lee, C., "A New Energy Harvester Design for High Power Output at Low Frequencies," *Sensors & Actuators: A. Physical*, vol. 199, pp. 344–352, 2013.

[14]   Abdelkefi, A., Najar, F., Nayfeh, A. H., and Ayed, S. Ben, "An Energy Harvester Using Piezoelectric Cantilever Beams Undergoing Coupled Bending–Torsion vibrations," *Smart Materials and Structures*, vol. 20, no. 11, pp. 1–11, 2011.

[15]   Erturk, A. and Inman, D. J., "A Distributed Parameter Electromechanical Model for Cantilevered Piezoelectric Energy Harvesters," *Journal of Vibration and Acoustics*, vol. 130, no. 41002, pp. 1–15, 2018.

[16]   Karami, M. a. and Inman, D. J., "Electromechanical Modeling of the Low-Frequency Zigzag Micro-Energy Harvester," *Journal of Intelligent Material Systems and Structures*, vol. 22, no. 3, pp. 271–282, 2011.

[17]   Karami, M. A. and Inman, D. J., "Parametric Study of Zigzag Micro-Structures for Vibrational Energy Harvesting," *Journal of Microelectromechanical Systems*, vol. 21, no. 1, pp. 145–160, 2012.

[18]   Karami, M. A. and Inman, D. J., "Analytical Modeling and Experimental Verification of the Vibrations of the Zigzag Microstructure for Energy Harvesting," *Journal of Vibration and Acoustics*, vol. 133, no. 11022, pp. 1–10, 2011.

[19]   Berdy, D. F., Srisungsitthisunti, P., Jung, B., Xu, X., Rhoads, J. F., and Peroulis, D., "Low-frequency Meandering Piezoelectric Vibration Energy Harvester," *IEEE Transactions on Ultrasonics, Ferroelectrics, and Frequency Control*, vol. 59, no. 5, pp. 846–858, 2012.

[20]   Karami, M. A., Yardimoglu, B., and Inman, D. J., "Coupled Out of Plane Vibrations of Spiral Beams for Micro-Scale Applications," *Journal of Sound and Vibration*, vol. 329, no. 26, pp. 5584–5599, 2010.

[21]   Robbins, W. P., Polla, D. L., and Glumac, D. E., "High-Displacement Piezoelectric Actuator Utilizing a Meander-ine Geometry," *IEEE Transactions on Ultrasonics, Ferroelectrics, and Frequency Control*, vol. 38, no. 5, pp. 454–460, 1991.

[22]   Fernandes, E., Martin, B., Rua, I., Zarabi, S., and Debéda, H., "Design , Fabrication , and Testing of a Low Frequency MEMS Piezoelectromagnetic Energy Harvester," *Smart Materials and*

Structures, vol. 27, no. 35017, pp. 1–15, 2018.

[23] Fernandes, E., Zarabi, S., Debéda, H., Lucat, C., Nairn, D., Wei, L., and Salehian, A., "Modelling and Fabrication of a Compliant Centrally Supported Meandering Piezoelectric Energy Harvester Using Screen-Printing Technology," in *Proceedings for the PowerMEMS2016; Journal of Physics: Conference Series (JPCS) vol.773,012109*, 2016.

[24] Leland, E. S. and Wright, P. K., "Resonance Tuning of Piezoelectric Vibration Energy Scavenging Generators Using Compressive Axial Preload," *Smart Materials and Structures*, vol. 15, no. 5, pp. 1413–1420, 2006.

[25] Apo, D. J., Sanghadasa, M., and Priya, S., "Low Frequency Arc-Based MEMS Structures for Vibration Energy Harvesting," in *Proceedings for Nano/Micro Engineered and Molecular Systems (NEMS)*, 2013, vol. 8, pp. 615–618.

[26] Sharpes, N., Abdelkefi, A., and Priya, S., "Two-Dimensional Concentrated-Stress Low-Frequency Piezoelectric Vibration Energy Harvesters," *Applied Physics Letters*, vol. 107, no. 93901, pp. 1–5, 2015.

[27] Paprotny, I., Leland, E. S., White, R. M., and Wright, P. K., "Optimization of a Die-Sized (10x10x4 mm 3) Mems Ac Energy Scavenger for Residential and Commercial Electricity End-Use Monitoring," *Proc. 10th Int. Workshop Micro Nanotechnol. Power Generat. Energy Convert. Appl.*, pp. 4–7.

[28] Brewer, J. A., "Low Resonant Frequency Beam Design for a Piezoelectric Energy Harvesting Device," Massachusetts Institute of Technology, 2005.

[29] Ibrahim, M. and Salehian, A., "Modeling , Fabrication , and Experimental Validation of Hybrid Piezo-Magnetostrictive and Piezomagnetic Energy Harvesting Units," *Journal of Intelligent Material Systems and Structures*, vol. 26, no. 10, pp. 1259–1271, 2015.

[30] Erturk, A., Tarazaga, P. a., Farmer, J. R., and Inman, D. J., "Effect of Strain Nodes and Electrode Configuration on Piezoelectric Energy Harvesting From Cantilevered Beams," *Journal of Vibration and Acoustics*, vol. 131, no. 11010, pp. 1–11, 2009.

[31] "LMS SCADAS Mobile: Siemens PLM Software," 2017. [Online]. Available: https://www.plm.automation.siemens.com/es/products/lms/testing/scadas/mobile.shtml.

[32] "75 lbf Dual Purpose Shaker | Excitation |The Modal Shop, Inc.," 2018. [Online]. Available: http://www.modalshop.com/excitation/75-lbf-Dual-Purpose-Shaker?ID=251.

[33] "PCB Model 352A24," 2018. [Online]. Available: http://www.pcb.com/Products/model/352A24.

[34]   "OFV-5000   Modular   Vibrometer,"   2018.   [Online].   Available: https://www.polytec.com/eu/vibrometry/products/single-point-vibrometers/ofv-5000-modular-vibrometer/.

[35]   "KJ   Laser   Micromachining,"   *WordPress   Developers*,   2014.   [Online].   Available: http://kjlasermicromachining.com/.

[36]   Pastor, M. and Binda, M., "Modal Assurance Criterion," *Procedia Engineering*, vol. 48, pp. 543–548, 2012.

[37]   Inman, D. J., "Vibration Testing and Experimental Modal Analysis," in *Engineering Vibration*, Third., New Jersey: Pearson Education, Inc., 2008, pp. 554–564.

[38]   Challa, V. R., Prasad, M. G., and Fisher, F. T., "A Coupled Piezoelectric–Electromagnetic Energy Harvesting Technique for Achieving Increased Power Output Through Damping Matching," *Smart Materials and Structures*, vol. 18, 2009.

[39]   Sharpes, N., Abdelkefi, A., and Priya, S., "Comparative Analysis of One-Dimensional and Two-Dimensional Cantilever Piezoelectric Energy Harvesters," *Energy Harvesting and Systems*, pp. 209–216, 2014.